remote sensing

Article

Performance of the Earth Explorer 11 SeaSTAR Mission Candidate for Simultaneous Retrieval of Total Surface Current and Wind Vectors

Adrien C. H. Martin [1,2,*], Christine P. Gommenginger [1], Daria Andrievskaia [2], Petronilo Martin-Iglesias [3] and Alejandro Egido [3]

[1] National Oceanography Centre, Southampton SO14 3ZH, UK; cg1@noc.ac.uk
[2] NOVELTIS, 31670 Labège, France; daria.andrievskaia@noveltis.fr
[3] European Space Research and Technology Centre (ESTEC), European Space Agency, 2201 AZ Noordwijk, The Netherlands; petronilo.martin.iglesias@esa.int (P.M.-I.); alejandro.egido@esa.int (A.E.)
* Correspondence: admartin@noc.ac.uk or adrien.martin@noveltis.fr

Abstract: Interactions between ocean surface currents, winds and waves at the atmosphere-ocean interface are key controls of lateral and vertical exchanges of water, heat, carbon, gases and nutrients in the global Earth System. The SeaSTAR satellite mission concept proposes to better quantify and understand these important dynamic processes by measuring two-dimensional fields of total surface current and wind vectors with unparalleled spatial and temporal resolution (1 × 1 km^2 or finer, 1 day) and unmatched precision over one continuous wide swath (100 km or more). This paper presents a comprehensive numerical analysis of the expected performance of the Earth Explorer 11 (EE11) SeaSTAR mission candidate in the case of idealised and realistic 2D ocean currents and wind fields. A Bayesian framework derived from satellite scatterometry is adapted and applied to SeaSTAR's bespoke inversion scheme that simultaneously retrieves total surface current vectors (TSCV) and ocean surface vector winds (OSVW). The results confirm the excellent performance of the EE11 SeaSTAR concept, with Root Mean Square Errors (RMSE) for TSCV and OSVW at 1 × 1 km^2 resolution consistently better than 0.1 m/s and 0.4 m/s, respectively. The analyses highlight some performance degradation in some relative wind directions, particularly marked at near range and low wind speeds. Retrieval uncertainties are also reported for several variations around the SeaSTAR baseline three-azimuth configuration, indicating that RMSEs improve only marginally (by ∼0.01 m/s for TSCV) when including broadside Radial Surface Velocity or broadside dual-polarisation data in the inversion. In contrast, our results underscore (a) the critical need to include broadside Normalised Radar Cross Section data in the inversion; (b) the rapid performance degradation when broadside incidence angles become steeper than 20° from nadir; and (c) the benefits of maintaining ground squint angle separation between fore and aft lines-of-sight close to 90°. The numerical results are consistent with experimental performance estimates from airborne data and confirm that the EE11 SeaSTAR concept satisfies the requirements of the mission objectives.

Keywords: total surface current vector; ocean surface vector wind; SAR; Doppler; along-track interferometry; Bayesian inversion; submesoscale dynamics; air–sea interactions

Citation: Martin, A.C.H.; Gommenginger, C.P.; Andrievskaia, D.; Martin-Iglesias, P.; Egido, A. Performance of the Earth Explorer 11 SeaSTAR Mission Candidate for Simultaneous Retrieval of Total Surface Current and Wind Vectors. *Remote Sens.* **2024**, *16*, 3556. https://doi.org/10.3390/rs16193556

Academic Editors: Ferdinando Nunziata, Weimin Huang and Martin Gade

Received: 1 August 2024
Revised: 20 September 2024
Accepted: 23 September 2024
Published: 24 September 2024

Copyright: © 2024 by the authors. Licensee MDPI, Basel, Switzerland. This article is an open access article distributed under the terms and conditions of the Creative Commons Attribution (CC BY) license (https://creativecommons.org/licenses/by/4.0/).

1. Introduction

The Earth's ocean is a complex, dynamic, living system that influences local and global weather, supports a wealth of marine life and ecosystems, delivers countless economic services, and plays a crucial role in regulating and mitigating climate change. Observing the spatial distribution and temporal evolution of ocean surface currents, winds and waves is vital to determine how the ocean transports, redistributes and exchanges water, heat, carbon, gases and other properties with other parts of the Earth System. Whilst ocean surface currents and winds are relatively well observed by spaceborne altimeters at large scales (effective resolution: 100 km, monthly [1]) and by scatterometers (effective spatial resolution of 20 km [2]), there is a pressing need for new high-resolution synoptic mapping capability to observe and quantify the dynamic processes that control interactions and exchanges of the ocean with the atmosphere, land and the cryosphere at shorter scales. Concurrent measurements of ocean surface winds, currents and waves are particularly relevant to validate and refine predictive Earth System Models and reduce uncertainties in forecasts and climate predictions.

The strong coupling of currents, winds and waves at the air–sea interface, and the spatial heterogeneity and high space-time variability of these phenomena, motivate the need to image these properties simultaneously, at high resolution. This has so far been difficult to achieve. Ocean surface wind measurements are abundant, mainly thanks to satellite scatterometers, but the spatial resolution is relatively coarse, data quality degrades near land and ice, and wind measurements are seldom coincident with total surface current data. In general, measurements of total ocean surface current vectors are scarce, particularly in the open ocean. Geostrophic currents (resulting from the balance between the Earth's rotation and pressure differences) can be estimated from satellite altimeter data, but these do not include currents caused by tides, wind, inertial motions, wave-induced Stokes drift, etc. Where total surface currents are measured, e.g., with drifters, Acoustic Doppler Current Profilers, or HF radars, the data are often limited by their spatial resolution, temporal sampling and/or spatial extent. These observational gaps have motivated recent advances in spaceborne remote sensing technology, particularly microwave Doppler radar systems, with developments including missions concepts like SKIM [3], WaCM [4], Harmony [5], SeaSTAR [6] and OdySea [7].

Amongst those, SeaSTAR (Sea Squinted Three-Azimuth Radar) is a groundbreaking satellite mission concept developed as a candidate for the European Space Agency Earth Explorer 11 program (EE11). The EE11 SeaSTAR concept aspires to revolutionise our ability to observe fast-evolving small-scale currents, winds and waves across all coastal seas, shelf seas and Marginal Ice Zones (MIZs) around the world [6,8]. SeaSTAR proposes to map two-dimensional vector fields of Total Surface Current Vectors (TSCV) and Ocean Surface Vector Winds (OSVW), simultaneously, over a wide swath, with unrivalled spatial resolution, precision, sensitivity and temporal revisit. In addition, SeaSTAR's TSCV and OSVW data would be augmented by concurrent collocated observations of Directional Ocean Wave Spectra (DOWS). Figure 1 shows the kind of 2D images of TSCV and OSVW vectorial fields that SeaSTAR would retrieve, providing observations on a regular 1 km × 1 km grid right up to the coast. In this example, the 150 × 150 km domain represents a typical SeaSTAR scene. Actual scenes will span several hundred kilometers along the track, with a swath width of 100 km wide or more.

SeaSTAR features several remarkable innovations, notably the utilisation of high-squint Synthetic Aperture Radar Along-Track Interferometry (SAR ATI), a state-of-the-art sensing technique so far never flown in space. Unlike the Earth Explorer 10 Harmony mission, SeaSTAR uses a single instrument on a single satellite to achieve high-precision interferometric acquisitions in two orthogonal squinted lines of sight, in addition to traditional broadside SAR imaging. With its unique three-azimuth configuration, SeaSTAR brings together the benefits of high-resolution high-precision SAR ATI imagers with the optimal azimuth diversity and wind direction sensitivity of advanced scatterometers like Metop-ASCAT.

Another innovation with SeaSTAR lies in the orbit. Through judicious altitude selection, EE11 SeaSTAR offers 1-day revisit throughout the mission, with the flexibility to shift (in-flight) between a fixed exact-repeat orbit, a slow-drifting and a very-slow-drifting orbit. This groundbreaking versatility empowers SeaSTAR to provide unique insight and understanding of fast-evolving small-scale ocean surface dynamics by observing the same spot repeatedly every day for extended periods, and even multiple times per day at some latitudes (crossovers).

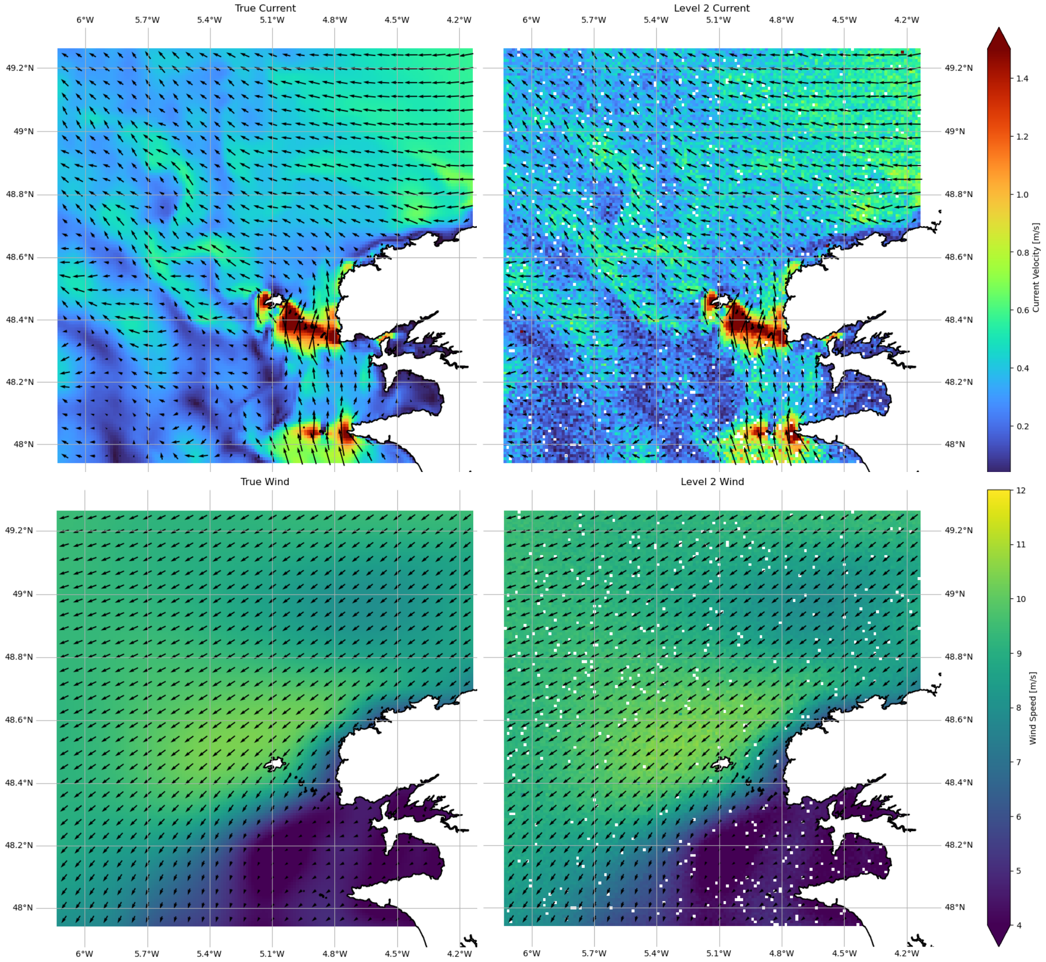

Figure 1. Example of SeaSTAR vectorial fields of (**top**) Total Surface Current Vectors (TSCV) and (**bottom**) Ocean Surface Vector Winds (OSVW) at 1 × 1 km^2 resolution on a typical 150 × 150 km^2 scene over Ouessant Island in the Iroise Sea, west of French Brittany. Left panels show the "true" TSCV and OSVW taken from the Coastal and Regional Ocean Community model (https://www.croco-ocean.org, accessed on 1 June 2023) that was input to the SeaSTAR simultaneous inversion presented in Section 3. Right panels show the retrieved 1 × 1 km^2 resolution Level-2 TSCV and OSVW output from the SeaSTAR simultaneous inversion. Small white dots are flagged data for which no viable minimum was found. These results are discussed in Section 4.2. Note the vectorial fields were sub-sampled to every 5 × 5 pixels for clarity.

Lastly, SeaSTAR developed a bespoke inversion algorithm that retrieves Total Surface Current Vectors and Ocean Surface Vector Winds simultaneously in a single step without prior information about winds or currents. The scheme was adopted as the SeaSTAR baseline Level-2 inversion algorithm during EE11 Phase 0 and forms the basis of the performance assessment presented in this paper.

The rest of the paper is structured as follows: Section 2 documents the main technical characteristics, observing geometry, instrument and Level-1 specifications of the EE11 SeaSTAR baseline concept used to evaluate the expected performance for TSCV and OSVW at Level-2. Section 3 presents the SeaSTAR simultaneous inversion scheme, detailing the Bayesian inversion framework, Geophysical Model Functions (used to forward model the Level-1 Normalised Radar Cross Section and Radial Surface Velocity data), the Ambiguity removal approach, and the sensitivity of the inversion to current and wind velocity and direction. The inversion builds on the approach of Martin et al. [9], updating the original framework to match the enhanced specifications of the EE11 SeaSTAR payload. The performance assessment results are presented in Section 4. Section 4.1 outlines the L2 performance in the idealised case of uniform wind and current fields, highlighting how performance varies across the swath and its degradation in some relative wind directions. Next, Section 4.2 presents the performance for realistic current and wind fields based on high-resolution numerical model data in the Iroise Sea. Finally, Section 4.3 reports the performance for different variations of the baseline instrument configuration. Discussion of the results and conclusions are given in Section 5.

2. SeaSTAR Technical Characteristics and Level-2 Requirements in EE11 Phase 0

SeaSTAR consists of a single instrument mounted on a single satellite flying in a Sun-Synchronous Low Earth Orbit. As the first mission of its kind, SeaSTAR carries an innovative multi-beam Synthetic Aperture Radar system operating at Ku-band (13.5 GHz) dedicated exclusively to high-squint along-track ocean interferometry over water surfaces. In EE11, Ku-band frequency was selected (in preference over Ka-band) as a trade-off between technology readiness and interferometric sensitivity. At Ku-band, a near-optimal along-track baseline can be accommodated on a single platform, delivering good interferometric sensitivity and high performance data across the swath for most wind conditions, including sheltered coastal regions.

The payload boasts two pairs of squinted interferometric SAR beams pointing around 45° in azimuth fore and aft of the satellite, and a standard side-looking (broadside) SAR beam (Figure 2). This ingenious arrangement delivers two near-orthogonal lines of sight of the ocean surface to achieve optimal ASCAT-like three-look azimuth diversity. This configuration enables simultaneous retrieval of the two vectorial components of both Total Surface Current Vectors (TSCV) and Ocean Surface Vector Winds (OSVW) in a single pass, with outstanding precision and spatial resolution. Moreover, the broadside beam has the potential to deliver multi-polarisation capability (VV/VH, HH/HV), although designs in EE11 Phase 0 could only accommodate VV polarisation in the broadside beam.

The SeaSTAR payload generates one continuous, one-sided off-nadir swath spanning a minimum of 100 km across-track (swath width goal: 150 km). The EE11 SeaSTAR baseline concept imposes a minimum incidence angle of 20° at near range in the broadside beam, which by geometry, implies incidence angles in the squinted directions between 31.5° (near) and 40° (far). For EE11 SeaSTAR, the azimuth look directions of the squinted directions varies across the swath, achieving ±45° mid-swath, and varying with a range from approximately ±52° (near) to ±38° (far) in both squinted beams. These baseline specifications (summarised in Table 1) are the result of the performance assessments presented in this paper, driven by the need to satisfy SeaSTAR's scientific requirements to achieve Level-2 uncertainties (RMSE) of 0.1 m/s and 1 m/s for TSCV and OSVW velocities, respectively, at 1×1 km^2 resolution. SeaSTAR observables are the Normalised Radar Cross Section (NRCS also known as σ^0) for the three beams and the Radial Surface Velocity (RSV) for the two squinted beams (+ for the broadside beam for experiments). Instrumental noise on NRCS is $\Delta\sigma_i^0 = k_{p_i} \times \sigma_i^0$ with k_{p_i} the radiometric resolution and σ_i^0 the NRCS of beam i. ΔRSV_i is the noise on RSV_i for beam i. Their values are given in Table 1.

Table 1. Key instrument specifications of the SeaSTAR payload in EE11 Phase 0.

	Near Range	Mid Swath	Far Range
In-swath distance	0 km	90 km	150 km
Broadside incidence	20.0°	28.4°	33.4°
Squint incidence	31.5°	36.5°	40.0°
Squint azimuth	52.2°	45.0°	37.8°

	Broadside direction	Squinted directions
Observables and Polarisation	NRCS VV	NRCS VV, RSV VV
NRCS k_{p_i}	4%	3%
ΔRSV_i	NA (or 0.2 m/s)	0.07 m/s

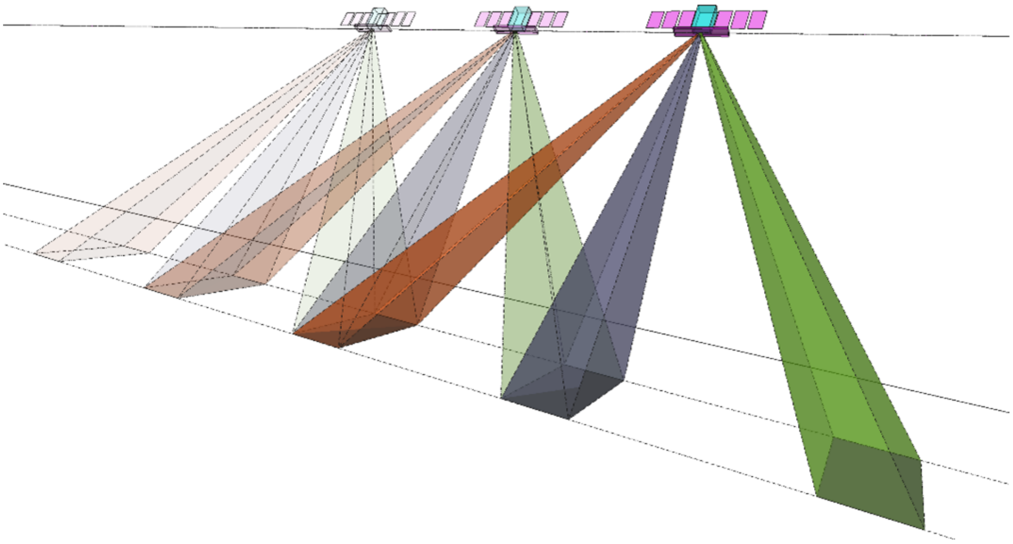

Figure 2. Schematic view of SeaSTAR's three-beam acquisition geometry, showing the satellite at three different moments in times to illustrate how the same ocean scene is viewed successively in three different lines-of-sight by the (green) FORE, (grey) MID and (red) AFT beams. In the FORE and AFT directions, the scene is observed by two SAR beams from the pairs of antennas separated along-track, each pair pointing FORE or AFT (not shown for clarity).

3. SeaSTAR Simultaneous Inversion Scheme

The SeaSTAR L2 retrieval algorithm follows the work of Martin et al. [9] and retrieves TSCV and OSVW simultaneously in one step, without the need for ancillary information. It is the objective of SeaSTAR to provide products derived solely from its own measurements, without dependence on external input. Outside a few instrumented sites, there are generally no reliable wind or current data at the fine spatial resolution targeted by SeaSTAR. Input from high-resolution ocean models or atmospheric models could be used, but suffer from a lack of validation, particularly in coastal, shelf seas and marginal ice zones.

Section 3.1 introduces the Bayesian theoretical framework for the inversion. Section 3.2 defines the cost function used in the minimisation. Section 3.3 describes the Geophysical Model Functions chosen to forward-model the Level-1 observables. Section 3.4 outlines how the ambiguity between multiple solutions is resolved. And Section 3.5 presents an analysis of the sensitivity of the inversion to wind and current conditions.

3.1. Bayesian Inversion with Maximum Likelihood Estimator

The inversion seeks to identify the wind and current vectors (OSVW, TSCV) that are most consistent with the Level-1 observables measured by the instrument: the Normalised Radar Cross Section (NRCS) also known as σ^0, and Radial Surface Velocity (RSV) in all available azimuth directions. We designate the state vector $\mathbf{x} = (\boldsymbol{u_{10}}, \boldsymbol{c})$ to represent OSVW and TSCV, and the observation vector $\mathbf{y} = (\boldsymbol{\sigma^0}, \mathbf{RSV})$ to represent the L1 observables.

The inversion problem consists of finding an estimate $\hat{\mathbf{x}}$ of the state vector $\mathbf{x}$ in the physical space with dimension N_{x}, given an observation vector $\mathbf{y}$ with dimension N_{y}. The observation operator, also known as the forward model or Geophysical Model Function (GMF), $\mathbf{H}$, relates the state vector $\mathbf{x}$ to the observables $\mathbf{y}$ through:

$$\mathbf{y} = \mathbf{H}(\mathbf{x})$$

Using the same approach as proposed in [10] and Stoffelen and Portabella [11], the objective is to maximise the conditional probability of the true physical state vector $\mathbf{x}$, given the observations $\mathbf{y}$:

$$P(\mathbf{x}|\mathbf{y}) = \int_{\Sigma} p_p(\mathbf{x}|\hat{\mathbf{x}}) p_o(\mathbf{H}(\hat{\mathbf{x}})|\mathbf{y}) d\hat{\mathbf{x}},$$

where the first and second terms in the integral, respectively, represent the uncertainty in the physical (p_p) and observation (p_o) domain. The integral is over the N_x-dimensional physical domain, i.e., a surface, Σ, defined by all possible physical states of the state vector $\mathbf{x}$. In our case, a surface is defined by all possible combinations of wind and current vectors.

If we assume that there are no errors in the physical space, including representativeness errors, $p_p(x|\hat{x})$ reduces to a Kronecker delta function (i.e., $\mathbf{x} = \hat{\mathbf{x}}$) so that the integral in the previous equation simply reduces to:

$$P(\mathbf{x}|\mathbf{y}) = P(\mathbf{H}(\hat{\mathbf{x}})|\mathbf{y}).$$

The problem now consists of solving $\mathbf{H}(\mathbf{x})$ to maximise $P(\mathbf{x}|\mathbf{y})$. Bayes' theorem states that:

$$P(\mathbf{x}|\mathbf{y}) = P(\mathbf{y}|\mathbf{H}(\hat{\mathbf{x}})) \cdot P(\mathbf{H}(\hat{\mathbf{x}}))$$

Thus, if $P(\mathbf{H}(\hat{\mathbf{x}}))$ is assumed constant, there remains only a single variable observation error term: $P(\mathbf{y}|\mathbf{H}(\hat{\mathbf{x}}))$. The assumption of constant $P(\mathbf{H}(\hat{\mathbf{x}}))$ is discussed in Section 3.5.

The estimated $\hat{\mathbf{x}}$ state vector as the value of $\mathbf{x}$ gives the maximum value of this probability. This is achieved by minimising the cost function:

$$\begin{aligned} J(\hat{\mathbf{x}}) &\propto -\ln p_o(\mathbf{y}|\mathbf{H}(\hat{\mathbf{x}})) \\ &\propto -\ln p_o(\mathbf{H}(\hat{\mathbf{x}}) - \mathbf{y}). \end{aligned}$$

Assuming p_o can be represented by a Gaussian distribution, we obtain the classic expression:

$$J(\hat{\mathbf{x}}) = (\mathbf{H}(\hat{\mathbf{x}}) - \mathbf{y})^T \mathbf{O}^{-1} (\mathbf{H}(\hat{\mathbf{x}}) - \mathbf{y}), \tag{1}$$

where $\mathbf{O}$ is the observation error covariance matrix. The observation errors include instrument errors and forward model errors. In our case, $\mathbf{O}$ is the combination of the error covariance matrix of NRCS ($\mathbf{S}$) and RSV ($\mathbf{D}$), i.e.:

$$\mathbf{O} = \begin{pmatrix} \mathbf{S} & \mathbf{C^T} \\ \mathbf{C} & \mathbf{D} \end{pmatrix}$$

with $\mathbf{C}$ the error covariance between NRCS and RSV. As performed in other past studies, e.g., [9,12,13], we assume NRCS and RSV observations are independent; hence, $\mathbf{C} = 0$, $\mathbf{S}$ and $\mathbf{D}$ are diagonal, as well as $\mathbf{O}$.

3.2. Cost Function Definition

Under the Bayesian framework and assumptions outlined in Section 3.1, the cost function is defined for subsequent minimisation using least-square fitting to determine the wind and current vectors that are most consistent with the SeaSTAR Level-1 observables (NRCS and RSV in available azimuth directions). The cost function selected for EE11 SeaSTAR has a similar form to that proposed in [9], but updated to suit the EE11 SeaSTAR configuration:

$$\begin{aligned} J(\hat{\mathbf{x}}) = J(\boldsymbol{u_{10}}, \boldsymbol{c}) =& \frac{1}{N_S + N_D} \sum_{i=1}^{N_S} \left(\frac{KuMod(\boldsymbol{u_{10}}, \chi_i, p_i) - \sigma^0_{obs,i}}{\Delta\sigma^0_i} \right)^2 \\ &+ \frac{1}{N_S + N_D} \sum_{i=1}^{N_D} \left(\frac{KuDop(\boldsymbol{u_{10}}, \chi_i, p_i) + c_{\|_i} - RSV_{obs,i}}{\Delta RSV_i} \right)^2 \end{aligned} \tag{2}$$

with i the beam index (e.g., fore, mid VV, mid HH, aft), $\boldsymbol{u_{10}}$ and $\boldsymbol{c}$, respectively, the OSVW (u_{10}, φ_u) and TSCV (c, φ_c). χ_i and p_i are, respectively, the azimuth direction and polarisation (e.g., VV) of beam i. The term $c_{\|_i} = |\boldsymbol{c}| \cdot \cos(\varphi_c - \chi_i)$ is the component of TSCV flowing in direction φ_c projected in the azimuth direction χ_i of beam i.

KuMod and *KuDop* are the Geophysical Model Functions to forward model the NRCS and the Wind-induced Artefact Surface Velocity (WASV, also known as Wave Doppler; [14])

at the chosen radar frequency (here Ku-band) for the relevant geometry and environmental conditions. $\sigma^0_{obs,i}$ and $RSV_{obs,i}$ are, respectively, the measured NRCS (linear units) and RSV (m/s) for beam i with azimuth direction χ_i and polarisation p_i. $\Delta\sigma^0_i$ and ΔRSV_i are the instrument errors (standard deviations) on, respectively, the measured NRCS and measured RSV for beam i with azimuth direction χ_i and polarisation p_i. N_S and N_D correspond, respectively, to the number of observations for NRCS and RSV from available beams.

3.3. Geophysical Model Functions for NRCS and RSV

3.3.1. Geophysical Model Functions for NRCS

At moderate to high incidence angles, the Normalised Radar Cross Section (NRCS) of the ocean is typically modelled as a function of wind speed, wind direction relative to the radar line-of-sight, incidence angle, radar wavelength and polarisation. For Ku-band NRCS, several Geophysical Model Functions (GMFs) exist in the literature, including NSCAT-2 [15], Ku-2011 [16], NSCAT-4 [17] and NSCAT-4DS [18]. Previously, Martin et al. [9] used NSCAT-2. The NSCAT-4 GMF represented an advance on NSCAT-2 GMF, and NSCAT-4 was itself recently superseded by NSCAT-4DS, which improved consistency for both wind Direction and Speed (hence the DS extension). The NSCAT-4DS GMF is used in most of the near-real-time Ku-band scatterometer wind products produced by the OSI SAF and is available as a Python script (https://scatterometer.knmi.nl/nscat_gmf/, accessed on 1 June 2023). Thus, NSCAT-4DS is the GMF for NRCS used in this paper, denoted hereafter as $KuMod$.

The top panels in Figure 3 illustrate the dependencies of NSCAT-4DS NRCS on (left) relative azimuth angle and (right) wind speed. Line colour indicates different incidence angles (20°, 30° and 40°). In the top-left panel, line thickness indicates wind speeds of 5, 9 and 15 m/s. In the top-right panel, thick and thin lines refer to VV and HH polarisation, respectively, and solid and dashed lines represent upwind and crosswind directions.

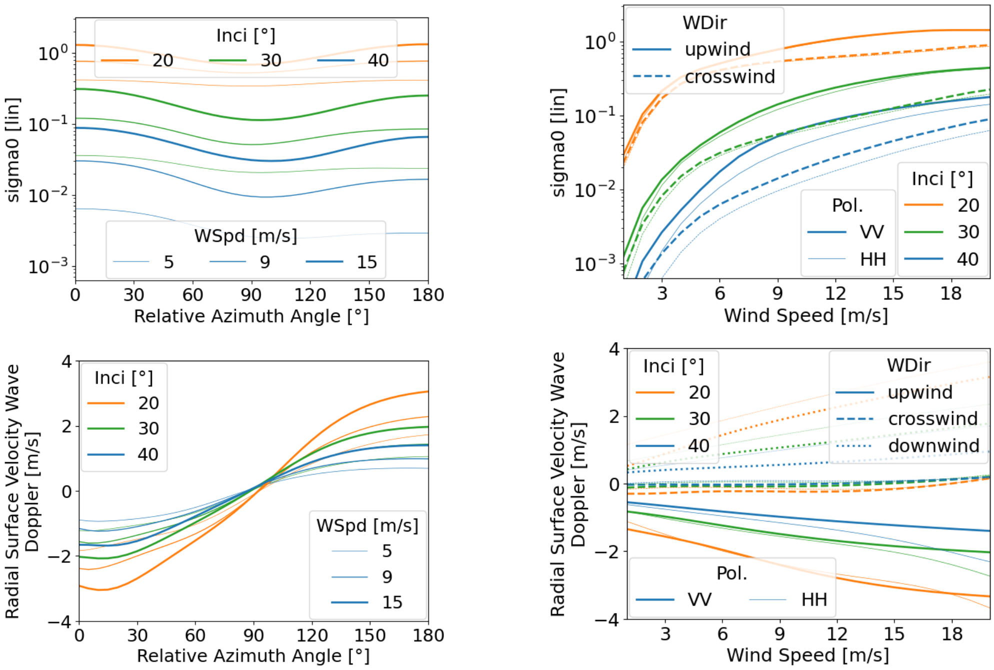

Figure 3. Geophysical Model Functions for (**top**) NRCS and (**bottom**) RSV Wind-wave induced Artefact Surface Velocity showing the dependence on (**left**) relative azimuth wind direction and (**right**) wind speed. Upwind is 0°. Downwind is 180°. Line colours represent incidence angles (20°, 30° and 40°). On the left panels, line thickness represents wind speed (5, 9 and 15 m/s). On the right panels, solid, dashed and dotted lines refer to upwind, crosswind and downwind. Thick and thin lines correspond to VV and HH polarisation.

The figures indicate that the dominant factors influencing NRCS are incidence angle and wind speed. NRCS decreases rapidly with increasing incidence angle, particularly at low wind speeds. For a given incidence angle, NRCS rises sharply with wind speed while exhibiting a weak modulation (≈20%) by wind direction. NRCS values are highest upwind (0°) and downwind (180°) when the radar line-of-sight is aligned with/against the wind, and lowest when the radar looks perpendicular to the wind (90°, crosswind). For incidence angles below 30°, there is little difference between VV and HH polarisation, suggesting limited benefits from multi-polarisation NRCS data closer to nadir.

3.3.2. Geophysical Model Function for RSV

The Radial Surface Velocity (RSV) sensed by microwave radars through the Doppler shift (in frequency or phase) relates to the velocity of the ocean surface relative to the platform projected in the radial line of sight of the radar. Once corrected for platform motion, the residual RSV consists of two parts: an ocean surface velocity representing the component of the TSCV in the radar line-of-sight projected in the slant range of the instrument ($c_{\|_i} = |\boldsymbol{c}| \cdot \cos(\phi_c - \chi_i)$ in Equation (2)); and a microwave scattering velocity, known as the Wind-wave Artefact Surface Velocity (WASV, [14]) or Wave Doppler (WD), which is caused by the motion of the surface scatterers responsible for the backscatter and does not contribute to water mass displacement. Both parts of the RSV appear explicitly in Equation (2). The WASV is denoted by $KuDop$.

There are currently three main GMFs in the literature to model the WASV, including Mouche et al. [12] (also known as C-Dop), Yurovsky et al. [19] and Moiseev et al. [20,21]. The C-Dop model [12] was derived empirically from Envisat ASAR Doppler Centroid Anomaly data at C-band (5.4 GHz) over the global ocean. The WASV is parameterised as a function of wind speed, wind direction, incidence angle and polarisation. Conversely, Yurovsky et al. [19] propose a semi-empirical model based on Ka-band Doppler scatterometer data (37.5 GHz) acquired from a sea platform in the Black Sea. It offers a simple parameterisation as a function of wind speed, wind direction and incidence angle, as well as a more advanced formulation that also accounts for sea state parameters like significant wave height and the frequency of wind sea and swell. The Yurovsky et al. [19] GMFs are applicable for radar frequencies from Ka-band to C-band. Finally, Moiseev et al. [20,21] is built from C-band Sentinel-1 Radial Velocity data. Like Yurovsky et al. [19], it provides a simple parameterisation with wind vector and incidence angle, as well as more advanced formulations with sea state dependencies. Unlike Mouche et al. [12] and Yurovsky et al. [19], the Moiseev et al. [20,21] algorithm is not publicly available.

No GMFs specially developed for Ku-band WASV currently exist in the literature. However, there is theoretical, e.g., [22] and empirical, e.g., [14,23] evidence that the WASV is not strongly radar frequency dependent. Yurovsky et al. [19] demonstrated the applicability and validity of their formulation to many observations published in the literature obtained with different systems at different radar frequencies from Ka-band to C-band. Recent analyses by Martin et al. [24] of Sentinel-1 C-band Radial Velocity data against HF radar data confirm that the Yurovsky et al. [19] GMF is the most suitable model to retrieve unbiased ocean surface currents from C-band SAR. However, due to computational time considerations when minimising the cost function in Equation (2), the Mouche et al. [12] GMF is used in this study.

The bottom panels in Figure 3 illustrate the dependence of the WASV on (left) relative azimuth angle and (right) wind speed for incidence angles of 20°, 30° and 40° (colours). Curves use the same legend as in the NRCS panels, except for the addition of downwind results as dotted lines in the bottom-right panel. We see that the WASV can reach very large values, as much as ± 3 m/s depending on wind direction, speed and incidence angle, matching or even exceeding the magnitude of strong ocean surface currents. The primary factor on the WASV is wind direction, reaching maximum magnitudes in the upwind and downwind directions and zero crosswinds. Wind speed and incidence angle are secondary effects on the WASV magnitude, increasing only slowly with wind speed. The WASV is markedly weaker at higher incidence angles, suggesting a preference for higher incidence angles. Interestingly, unlike NRCS, the WASV shows significant differences between VV and HH polarisation even at incidence angles within 20° of nadir (downwind).

3.4. Multiple Solution & Ambiguity Removal

As in scatterometry, the SeaSTAR minimisation can return up to four different solutions [25], leading to a well-known ambiguity problem. This issue received extensive attention in scatterometry, where mature ambiguity removal procedures now exist and have been implemented in operational processing centres to identify the most likely wind vector solutions [26]. Similar approaches could be used for SeaSTAR, although the full application of operational schemes to SeaSTAR data has yet to be tested. Instead, three simpler ambiguity removal approaches have so far been considered:

1. Deepest cost function minimum: in principle, the solution associated with the lowest cost value should identify the best solution. This method is very attractive as it depends solely on SeaSTAR data. However, the method is not 100% reliable and can sometimes return the wrong local minimum and give erroneous results depending on instrument noise levels ($\Delta\sigma$, ΔRSV) and in some relative wind directions.
2. A priori knowledge: in some cases, the cost function minima are associated with OSVW and TSCV that are physically unlikely for this region or conditions. In these cases, a priori knowledge of the likely magnitude or direction of TSCV or OSVW in this region may be sufficient to discriminate between ambiguous solutions and nudge the inversion towards the best solution.
3. Ancillary information from other sources: likewise, one could use ancillary information about the magnitude or direction of TSCV or OSVW from another satellite or a model to nudge the retrieval towards the best solution. As explained previously, this approach is not ideal since there are no reliable sources of information about TSCV and OSVW at the fine resolution considered by SeaSTAR.

We will not address the ambiguity removal problem in this paper. For the results in this paper, the ambiguity removal method is close to the second approach, but with perfect knowledge. The best solution among the ambiguities is identified by taking the solution that returns a current magnitude closest to the true current. Internal testing shows that results are broadly similar when selecting the solution closest to the true wind or closest to a combination of both wind and current. Further work is needed to determine the relative merits of different ambiguity removal schemes for SeaSTAR.

3.5. Sensitivity of the Inversion to TSCV and OSVW

In this section, we explore the impact of the inversion of the non-linearity of the forward models (GMFs) on TSCV and OSVW. Stoffelen and Portabella [11] emphasise that, for wind vector retrieval in scatterometry, artificial error accumulations can arise due to the instrument's reduced sensitivity in some wind directions. This sensitivity primarily stems from the viewing geometry, encompassing factors like azimuth diversity, incidence angles and polarisation.

Formally, in Equation (2), we assume a constant $P(\mathbf{H}(\hat{\mathbf{x}}))$, i.e., uniform distribution. Here, we test this hypothesis following the work of Stoffelen and Portabella [11] and Chi and Li [27]. We relate the probability density $p(\mathbf{H}(\hat{\mathbf{x}}))$ to $p(\mathbf{x})$ with $p(\mathbf{H}(\hat{\mathbf{x}})) = p(\hat{\mathbf{x}})\|\partial\mathbf{H}/\partial\hat{\mathbf{x}}\|$. For small changes in $\hat{\mathbf{x}}$ (current or wind), $p(\hat{\mathbf{x}})$ can be assumed uniform, and the probability density follows the total sensitivity of the forward model to the physical variables, $\|\partial\mathbf{H}/\partial\mathbf{x}\|$.

3.5.1. Sensitivity of the Inversion to TSCV

The sensitivity of the inversion to TSCV ($\boldsymbol{c}$) originated from the second term in Equation (2) and reduces to:

$$\left\|\frac{\partial \mathbf{H}}{\partial \boldsymbol{c}}\right\| = \frac{1}{N_{\mathrm{D}}}\sum_{i=1}^{N_{\mathrm{D}}}\left(\frac{1}{\Delta RSV_i}\frac{\partial c_{\|_i}}{\partial \boldsymbol{c}}\right)^2$$

If we assume $\Delta RSV_{broad} \gg \Delta RSV_{fore,aft}$ (RSV data much noisier in broadside than squinted directions), and considering that $c_{\|_i} = |\boldsymbol{c}| \cdot \cos(\varphi_c - \chi_i)$, where $\chi_{aft} - \chi_{fore} = 90°$, we find that the contribution from the broadside direction becomes negligible and that $\left\| \frac{\partial \mathbf{H}}{\partial \boldsymbol{c}} \right\|$ becomes constant regardless of current velocity and direction.

If the broadside RSV contribution cannot be ignored, it introduces anisotropy in the sensitivity to the current direction, weighted by the relative noise between the broadside and squinted RSV measurements. In other words, with this setup, the sensitivity of the retrieval to current velocity and direction is mathematically constant when the inversion is limited to data from two orthogonal squinted antennas.

3.5.2. Sensitivity of the Inversion to OSVW

The sensitivity of the inversion to OSVW ($\boldsymbol{u_{10}}$) originates from both terms in Equation (2) and contains dependencies on both wind speed and wind direction. Given the smooth monotonic dependence of $KuMod$ and $KuDop$ on wind speed seen in Figure 3, for small increments of OSVW, the sensitivity on wind speed can be assumed quasi-linear. It is therefore the sensitivity to wind direction that mainly determines the modulation of $P(\mathbf{H}(\hat{\mathbf{x}}))$. To simplify the analysis, we explore the sensitivity on the inversion to wind direction (φ_u) for NRCS and RSV separately, as well as the full combined sensitivity. Noise values on NRCS and RSV used to combine observables together are the ones listed in Table 1.

Following the method presented in Stoffelen and Portabella [11], Figure 4 represents the sensitivity to wind direction of (left to right) NRCS, RSV and fully combined, for (top to bottom) near, mid and far-range cells for light wind conditions with a wind speed of 5 m/s. In order to keep some generality, this figure uses a simplified geometry with a constant 45° squint angle on the ground across the swath. The results for variable squint angle across the swath are broadly similar and shown in Appendix A (Figures A1–A3). These figures in the appendix are for three different wind speed conditions of 5, 9 and 15 m/s. The focus here is on light wind speed conditions (5 m/s), which are the most difficult for the system due to low backscattered signal.

The total three-beam sensitivity of NRCS to wind direction ranges from 0.01 to 0.5 deg^{-2} (Figure 4-left, black) and shows strong modulation with the relative azimuth angle, with local maxima at 0° (i.e., satellite heading), 90°, 180° and 270° and minima when the wind direction is parallel to the squinted look directions (45°, 135°, 225°, 315°). To second order, the sensitivity increases with range with lower sensitivity at near range than at far range (Figure 4-top to bottom, black). When the range increases, the total NRCS sensitivity to wind direction improves only slightly when the wind is downwind for one of the squinted antennae (225°, 315°). The addition of the broadside antenna (green line) adds sensitivity to the local minima compared to the sensitivity with the two squinted beams (red line). The amplitude of this curve can be increased by improving the broadside radiometric resolution with a lower k_p. When the range increases, the sensitivity of the broadside antenna increases. This is the main reason why the requirements for SeaSTAR are pushed for a broadside incidence angle higher than 20°.

The total sensitivity of RSV to relative wind direction (Figure 4-middle column, black) shows a similar modulation with azimuth as NRCS but shifted by 90° and with an amplitude more than half smaller (note the scale is different). To first order, RSV sensitivity shows local minima at 0°, 90°, 180° and a significantly deeper minimum at 270° (downwind for the broadside antenna). RSV sensitivity maxima occur where NRCS sensitivity is minimum, i.e., at 45°, 135°, 225° and 315° when the wind is parallel to the squinted look directions. Contrary to the NRCS sensitivity, the RSV sensitivity decreases with range (Figure 4-middle column top to bottom).

The combined full sensitivity of NRCS and RSV to relative wind direction (Figure 4-right in red and purple) is dominated by the sensitivity of NRCS (in solid black) but with shallower minima. The full sensitivity varies little with the addition of RSV for the broadside (red versus purple lines). The local minima of the full sensitivity tend to be the same as for NRCS (45°, 135°, 225° and 315°) when the wind is blowing parallel to the squinted beam direction. There is a wide plateau of low sensitivity at near range for azimuth between 240° and 300°. The full sensitivity generally increases with range, except for the local minima around 240° and 300° for which the full sensitivity slightly decreases with a range from 0.07 deg^{-2} to 0.05 deg^{-2}. Sensitivity at 270° increases with range and is close to 0.2 deg^{-2} at far range.

From these results, we expect the performance for SeaSTAR to be degraded at near range over a range of wind direction relative to the satellite heading between about 240° and 300°, where the sensitivity is minimal.

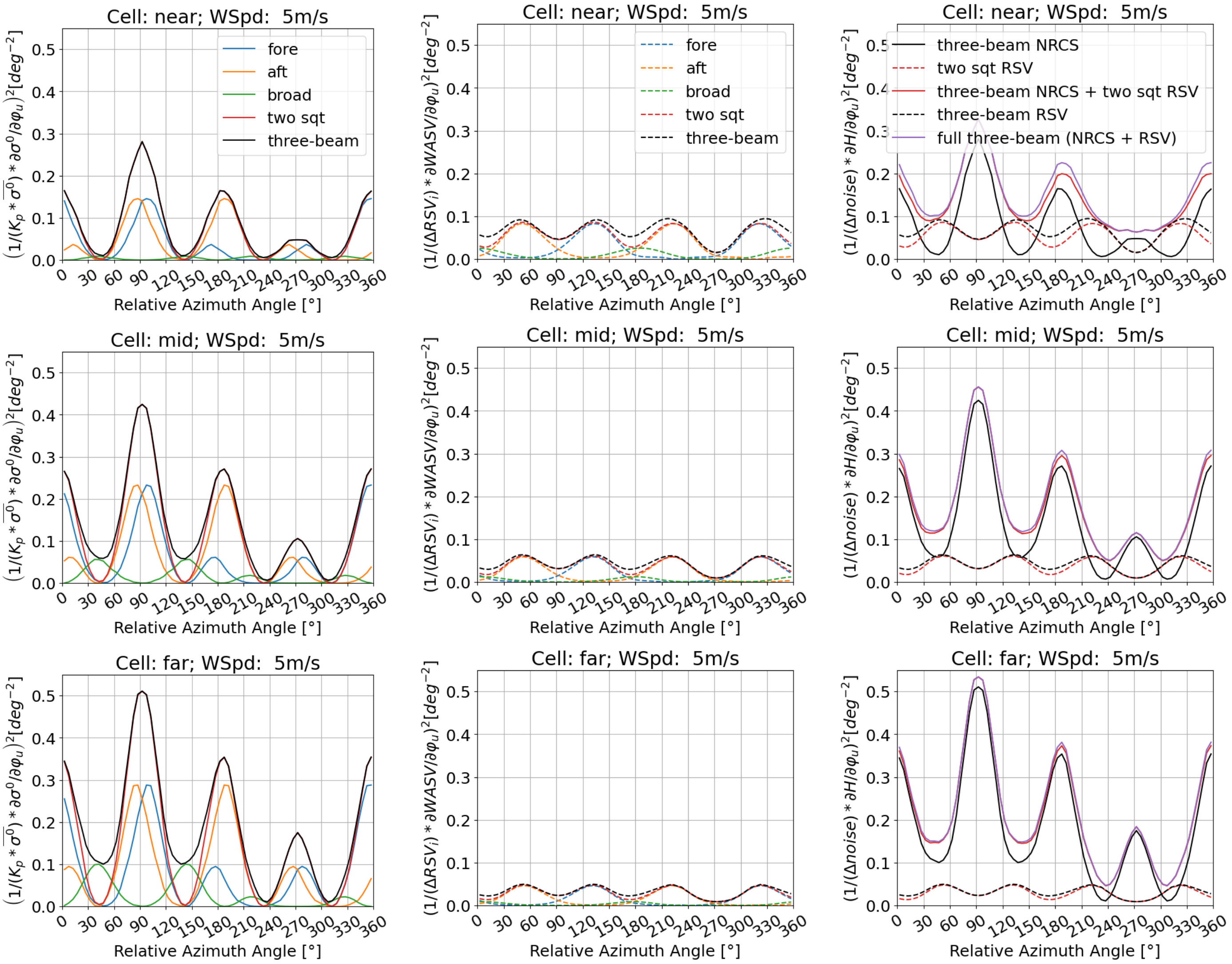

Figure 4. Sensitivity to relative wind direction of different terms of the inversion (**left**) NRCS ($\partial\sigma^0/\partial\varphi_u$), (**middle**) RSV ($\partial RSV/\partial\varphi_u$) and (**right**) full NRCS + RSV. φ_u denotes the wind direction relative to the satellite heading. The first, second and third rows show, respectively, sensitivity results at near, mid and far ranges. The satellite heading is (0°), the squinted antennas are oriented at 45° (fore) and 135° (aft) in azimuth. In the left and middle panels: blue, orange and green lines indicate the sensitivity with only the fore, only the aft and only the broadside direction; red indicates the sensitivity with the two squinted beams (fore + aft); in (**left**) and (**mid**) black lines indicate the total sensitivity with all three beams. In the **right** panels, black (plain and dashed) lines and the red dashed line are reproduced from the **left** and **mid** panels. The red and purple solid lines show, respectively, the sensitivity for combined three-beams NRCS plus squinted beams RSV and for the full three-beams (NRCS + RSV). The sensitivity is measured in degree^{-2}. Wind speed = 5 m/s.

4. SeaSTAR Level-2 Retrieval Performance for TSCV and OSVW in EE11 Phase 0

The simultaneous inversion scheme outlined in the previous section forms the core of the numerical framework devised to estimate the SeaSTAR Level-2 (L2) retrieval performance for different ocean current and wind conditions, instrument configurations, geometries and Level-1 (L1) noise specifications. The numerical framework is illustrated in Figure 5. Red boxes (top left) indicate input parameters linked to the instrument configuration, geometry and system performance. The blue box denoted 'Ocean data' (top right) represents the 'true' Total Surface Current Vectors and Ocean Surface Vector Winds used as input. These are fed into the Forward Models (GMFs) to generate noise-free Normalised Radar Cross Section (NRCS) and Radial Surface Velocity (RSV) data for each azimuth look direction and/or polarisation specified by the instrument configuration. White Gaussian noise with standard deviations $\Delta\sigma^0$ and ΔRSV is then added to NRCS and RSV data, respectively, to produce simulated Level-1B products (L1B, i.e., calibrated L1). The simulated L1B data (${\sigma^0}_i$, RSV$_i$) are input to the cost function minimisation module (Equation (2)) to find the best TSCV and OSVW solutions. The retrieval performance is evaluated by comparing the 'Retrieved L2 data' (blue box, bottom right in Figure 5) with the 'true' TSCV and OSVW 'Ocean data' (blue box, top right in Figure 5).

The EE11 Phase 0 SeaSTAR L2 performance was estimated for input ocean conditions representing idealised uniform current and wind fields (Section 4.1) and for realistic TSCV and OSVW fields shown in Figure 1 (Section 4.2). The metric used to estimate performance is the Root Mean Square Error (RMSE), defined as the difference between the retrieved and true field TSCV or OSVW. Three values of RMSE are computed, one for the vector using the two components of the vector and normalised by $\sqrt{2}$ [28], one for the velocity, and one for the direction. The direction RMSE is calculated as the square root of the sum of squares of the circular standard deviation and circular mean (as implemented in *scipy.stats v1.7.3* based on Fisher [29]).

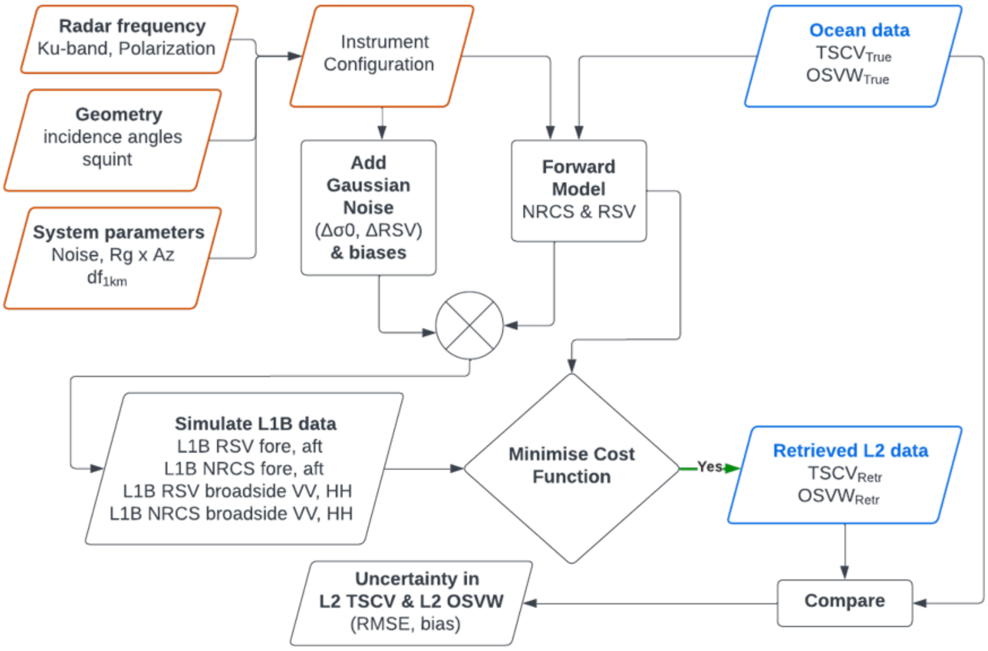

Figure 5. Numerical framework used to evaluate SeaSTAR Level 2 retrieval performance in EE11 Phase 0.

4.1. SeaSTAR Level-2 Retrieval Performance for Idealised Uniform TSCV and OSVW

In this section, the instrument configuration parameters are those set up in Table 1. The 'true' ocean input data consist of uniform fields of TSCV and OSVW that are constant in magnitude and direction over the full swath. The results are presented for a constant

TSCV field of 0.6 m/s flowing to 150 degrees and a constant wind speed of 5 m/s. Given the sensitivity of the retrieval to wind direction highlighted in Section 3.5, the analysis is repeated for the full range of wind directions (0°–359°) varying in 15° steps. The satellite heading is North (0°), the squinted antennas are oriented at 45° (fore) and 135° (aft) in azimuth. The instrument three-beam orientation relative to wind vectors is shown in the inset in Figure 6-left.

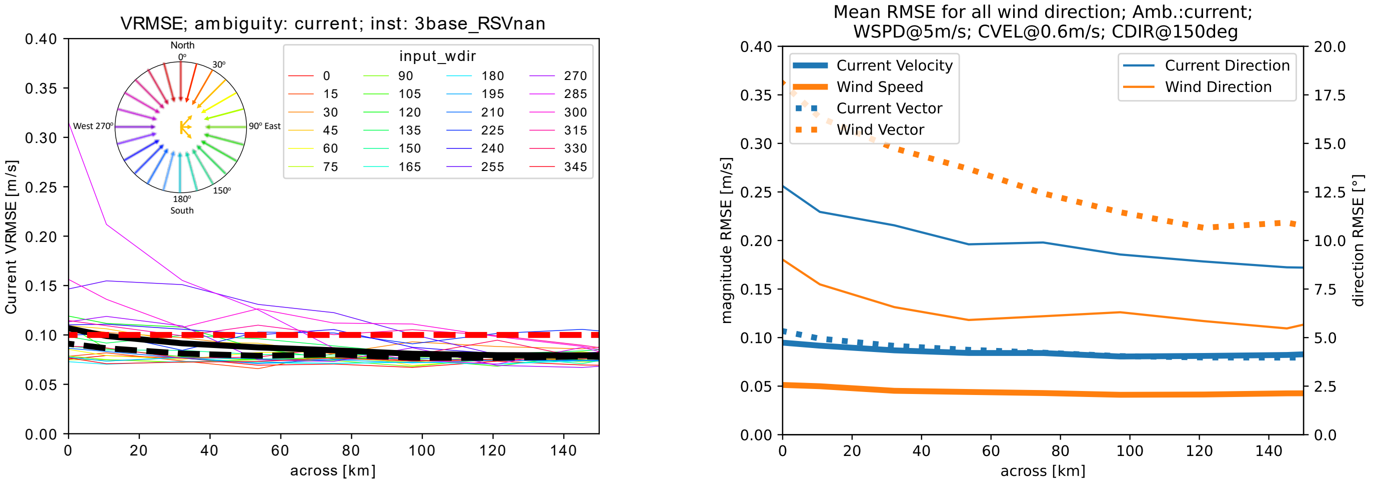

Figure 6. (**Left**) SeaSTAR simulated performance in EE11 Phase 0 for L2 TSCV at 1 km^2 for idealised uniform TSCV and OSVW input fields, shown as RMSE of TSCV across the swath for different wind directions (coloured lines). Input TSCV is 0.6 m/s flowing to 150 degrees, OSVW is constant 5 m/s. The colour wheel inset shows the SeaSTAR three look directions relative to different wind vectors. Instrument specifications are those in Table 1. The thick dotted red line indicates the 0.1 m/s mission requirement for L2 TSCV at 1 km^2. The thick solid and dashed black lines are the mean and median RMSE for TSCV averaged over all wind directions. (**Right**) SeaSTAR simulated performance in EE11 Phase 0 for L2 TSCV and OSVW at 1 km^2 shown as the mean RMSE (averaged over all wind directions) across the swath for TSCV and OSVW velocity, vector (left y-axis) and direction (right y-axis). Blue lines relate to TSCV, orange lines to OSVW. Thick, dotted and thin lines represent RMSE of vector, velocity and direction.

Here, the input wind field corresponds to an Earth Relative Wind (ERW); hence, the Ocean Surface Vector Wind (OSVW) used to generate the NRCS observables is the vector difference of this ERW with the TSCV. Across the range of ERW directions, the OSVW speed varies from 4.4 m/s (ERW direction of 330° aligned with TSCV) to 5.6 m/s (ERW direction of 150° opposite to TSCV). Note the 180° shift between wind and current direction conventions: wind direction refers to where the wind is coming from; current direction refers to where the current is going. The change in OSVW direction relative to ERW is maximum (up to ±6.8°) when wind is blowing perpendicular to TSCV (i.e., 60°, 240°).

The results for these simulations are presented in Figure 6-left as a function of across-track distance (range) in the swath. The thick dashed red line indicates the 0.1 m/s L2 TSCV uncertainty requirement for the EE11 SeaSTAR mission. The TSCV RMSE obtained for different constant wind directions are shown by different coloured lines. The thick solid black line represents the mean TSCV RMSE averaged over all wind directions (thick dashed black line is the equivalent using median). We find that the L2 TSCV uncertainty for the proposed concept is compliant with the mission's L2 requirement across the full swath if considering the median RMSE (thick dashed black line), and for most of the swath (from 10 km across-track) if considering the mean RMSE (thick solid black line).

Individual coloured lines in Figure 6-left indicate degraded L2 performance, particularly at near range, for some wind directions around 270° (e.g., 255°, 285°, 300°). This was anticipated from the results in Section 3.5, which showed reduced sensitivity for directions between 240°–300°. From Section 3.5, one could expect the TSCV L2 performance to show symmetry about 270° (Figure 4-top-right), i.e., the same degraded performance for wind directions of 255° and 285°, or 240° and 300°. This is not the case here because the TSCV changes the Ocean Surface Vector Wind (OSVW, relative to the ocean surface), reducing it by about 0.5 m/s when the wind is from (285°, 300°) and turning all OSW directions around 270° slightly southward (by about 5°).

The mean RMSE (averaged over all wind directions) of TSCV and OSVW across the swath are summarised in Figure 6-right. Blue lines relate to TSCV, and orange lines to OSVW. Thick solid lines are RMSE for TSCV and OSVW velocities, thick dashed lines for TSCV and OSVW vectors (left vertical axis), and thin solid lines for TSCV and OSVW directions (right vertical axis). The thick dashed blue line is the same as the thick black line in Figure 6-left. As noted previously, the mean RMSE for TSCV satisfies the 0.1 m/s mission requirement for L2 TSCV at 1 km^2 resolution. For OSVW (dashed orange line in Figure 6-right), the RMSE is better than 0.4 m/s, achieving a similar or better performance as is currently possible with scatterometers but at 1 km^2 resolution. These results demonstrate that the SeaSTAR instrument concept proposed in EE11 Phase 0 (Table 1) satisfies the scientific requirements of the mission for Level-2 performance for TSCV and OSVW at 1 km^2 spatial resolution.

4.2. SeaSTAR Level-2 Retrieval Performance for Realistic TSCV and OSVW in the Iroise Sea

Figure 1-left presents the TSCV and OSVW fields in the Iroise Sea, west of French Brittany, used to estimate the SeaSTAR L2 performance in realistic current and wind conditions. The area is characterised by intense tidal currents and current gradients steered by bathymetry through narrow gaps between islands and the mainland. The area near Ouessant Island was also the site of the first scientific campaign of the SeaSTAR airborne demonstrator known as OSCAR (Ocean Surface Current Airborne Radar) carried out in Iroise Sea in May 2022 [30]. The 'true' realistic ocean input data shown in Figure 1-left were taken from the high-resolution TSCV and OSVW fields of the CROCO model (Coastal and Regional Ocean Community model; https://www.croco-ocean.org) obtained via Ifremer. CROCO is an ocean model system that aims to resolve very fine-scale processes, especially in coastal areas, and their interactions with larger scales. The model provides hourly output on 1 km^2 grid cells. The snapshot used here (Figure 1-left) displays strongly variable TSCV between 0.2 and 1.2 m/s flowing to the North, North-West or West, and relatively homogeneous slow-varying OSVW except for a sharp north to south gradient from ≈10 m/s north-easterlies to ≈4 m/s north-north-easterlies. The area covers 150 × 150 km^2 which corresponds to the typical dimensions of the planned SeaSTAR acquisitions (goal).

Using the approach described at the beginning of Section 4, simulated L1B images of NRCS (σ^0) and Radial Surface Velocities (RSV) were produced for the fore, broadside and aft lines-of-sight (see Figure 7) for the instrument configuration and specifications in Table 1. The simulated NRCS images in the three azimuth lines-of-sight (Figure 7-left) correctly show reduced backscatter in the area of low wind speeds south of Ouessant Island (around 48.2°N-5.1°W). NRCS from the broadside beam (MidV, Figure 7-mid-left) are generally higher than in the fore and aft directions because the broadside beam observes the surface at steeper incidence angles. The aft NRCS image (Figure 7-bottom-left) appears darker than the fore NRCS image (Figure 7-top-left), reflecting the fact that the aft line-of-sight is orthogonal to the wind (crosswind) whereas the fore beam is looking upwind.

For the simulated L1B images of RSV, the interpretation in the three azimuth directions is more complicated due to the combined effect of the current projected in each beam's line-of-sight and the Doppler wave bias (also known as the Wind-wave Artefact Surface velocity; WASV, [14]) in each line-of-sight. For the given wind and current fields, we find that large-scale variations in RSV are due mainly to the WASV, whereas small-scale variations are dominated by the currents.

The retrieved L2 TSCV and OSVW obtained as the output of the SeaSTAR simultaneous inversion is shown in Figure 1-right, revealing SeaSTAR's extraordinary ability to recover the structure and magnitude of complex TSCV and OSVW fields with unparalleled levels of detail and accuracy. The small white dots in Figure 1-right correspond to pixels where the inversion could not find a viable solution close enough to the observables. For now, these pixels are simply flagged out, but more work is needed to resolve this issue better in the future. Over the full domain, the comparison between retrieved and true fields returns a vector RMSE for TSCV and OSVW better than 0.1 m/s and 0.4 m/s, respectively. The Pearson correlation coefficient between retrieved and true values of TSCV is 0.89 for both meridional and zonal components, and 0.98 and 0.92 for the OSVW meridional and zonal components, respectively.

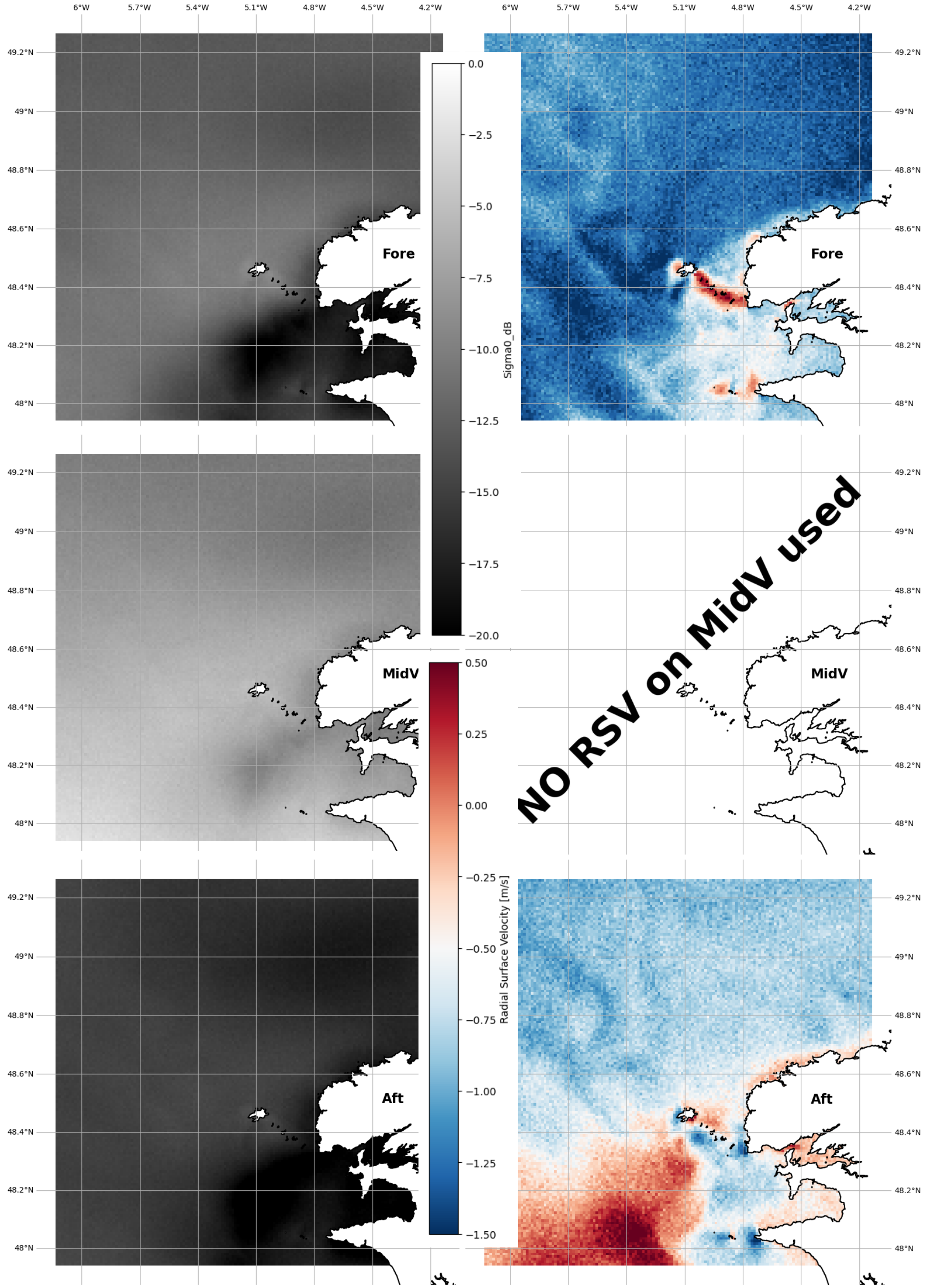

Figure 7. SeaSTAR simulated L1B images for realistic currents and winds in Iroise Sea near Ouessant for the (**top**) fore, (**middle**) broadside and (**bottom**) aft lines-of-sight. (**Left**) Simulated L1B images of Normalised Radar Cross Section (**Right**) Simulated L1B images of Radial Surface Velocity. Instrument configuration and specifications are shown in Table 1.

4.3. SeaSTAR Level-2 Retrieval Performance for Different SeaSTAR Instrument Specifications

In this final section, we report the retrieval performance obtained with different variations of the SeaSTAR instrument configuration explored during EE11 Phase 0. These analyses quantify the impact on the performance of various instrument trade-offs and serve to refine the requirements on the mission and payload design for industry in EE11 Phase 0.

Six instrument configurations are presented, centred and derived from the SeaSTAR 'baseline' configuration described and evaluated in previous sections (e.g., Table 1). Details of each configuration are given below. In addition, the performance is estimated for a wider swath extended by 50 km towards the near range to quantify performance also at incidence angles below 20° from nadir. The near-range swath extension is indicated by negative range values from -50 km to 0 km, where 0 km represents the near-range edge of the swath for the baseline design. Table 2 summarises the across-track distances, incidence and azimuth angles of the broadside and squinted beams for this near-range extended swath.

Table 2. SeaSTAR instrument specifications for the EE11 Phase 0 Baseline (**3base_RSVnan**) and the Squint 29 (**3sq29_RSVnan**) configurations (see Section 4.3).

In-Swath Across-Track Distance		**−50 km**	**0 km**	**50 km**	**100 km**	**150 km**
Broadside incidence angle	Baseline Squint 29	15.3° 25.0°	20.0° 28.1°	24.7° 31.2°	29.2° 34.4°	33.4° 38.1°
Squint incidence angle	Baseline Squint 29	28.7°	31.5°	34.3°	37.1°	40.0°
Squint azimuth angle	Baseline Squint 29	56.2° 31.0°	52.2° 29.0°	48.2° 27.0°	43.2° 24.9°	37.8° 22.5°

As was performed in Figure 6-right, performance is reported as the mean RMSE (averaged over all wind directions) across the swath. Since TSCV performance represents a stronger mission driver than OSVW, the focus is on mean RMSE for TSCV. Environmental conditions are the same as in Section 4.1, i.e., constant TSCV field of 0.6 m/s flowing to 150 degrees and a constant wind speed of 5 m/s, repeated for the full range of wind directions (0°–359°) varying in 15° steps.

The mean RMSE for TSCV across the extended swath is presented in Figure 8 for the six instrument configurations, the labels in the legend referring to the following configurations:

3base_RSVnan: this is the baseline SeaSTAR configuration described in Table 1 put forward at the end of the EE11 Phase 0. It has three azimuth lines-of-sight (fore, broadside, aft), measuring $NRCS_{VV}$ broadside, $NRCS_{VV}$ and RSV_{VV} in squinted fore and aft directions, and squinted L1B ΔRSV_{VV} of 0.07 m/s.

3base_RSV40: same as the baseline but with additional RSV_{VV} broadside, with broadside L1B ΔRSV_{VV} = 0.4 m/s.

2base: same as the baseline but with no broadside capability (two-azimuth configuration).

4base_RSVnan: same as the baseline but with additional $NRCS_{HH}$ broadside with the exact same geometry and noise as $NRCS_{VV}$. No broadside RSV_{VV} nor RSV_{HH}.

4base_RSV40: same as **4base_RSVnan** but with broadside RSV_{VV} and broadside RSV_{HH} with broadside L1B $\Delta RSV_{VV} = \Delta RSV_{HH} = 0.4$ m/s.

3sq29_RSVnan: same as the baseline but with a smaller squint angle. Incidence angles in the squinted directions are the same as for the baseline, but azimuth angles are smaller. At a given range, incidence angles in the broadside direction sample are larger when squint is smaller. The ranges, incidence and azimuth angles across the swath for the baseline and this configuration are given in Table 2.

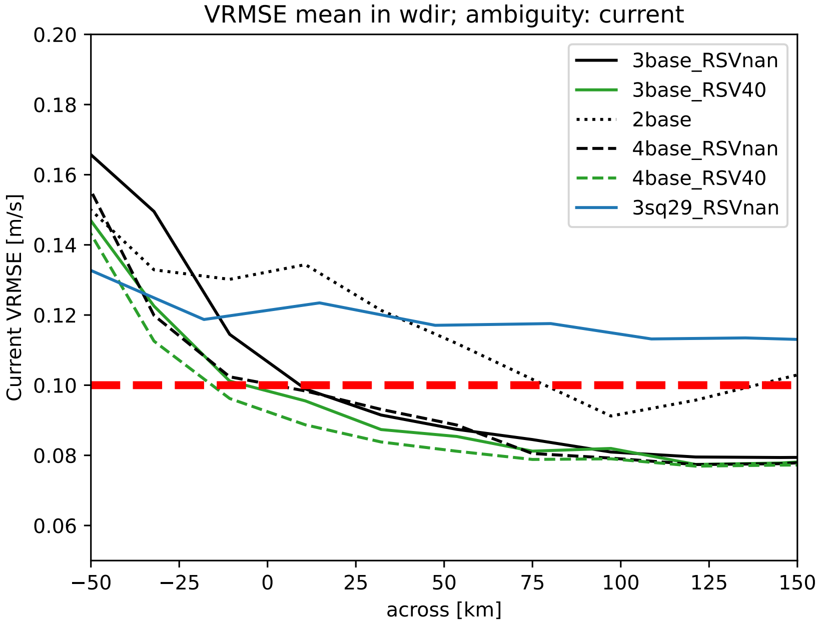

Figure 8. SeaSTAR simulated performance in EE11 Phase 0 for L2 TSCV at 1 km^2 shown as the mean RMSE (averaged over all wind directions) across the swath for TSCV vector for different SeaSTAR instrument configurations. The red dashed line represents the 0.1 m/s mission requirements for TSCV. Different instrument configurations are identified by the labels in the legend and described in Section 4.3.

In Figure 8, the TSCV performance across the swath is indicated for the baseline solution by the black solid line. We find that all four "3base" and "4base" configurations report performances similar to the baseline, and all four configurations satisfy the 0.1 m/s mission requirements for TSCV (red dashed line) over most of the 0–150 km swath. However, performances deteriorate rapidly at near range [−50 km, 0 km] and do not satisfy the 0.1 m/s mission requirement for TSCV when incidence angles fall below 20°.

Compared to the baseline (3base_RSVnan, black solid line), the addition of broadside $NRCS_{HH}$ (4base_RSVnan, black dashed line) leads to small RMSE improvements at near range (reduction of ∼0.01 m/s at 0 km, ∼0.03 m/s at −30 km) and only marginal improvements at ranges above 10 km (<0.01 m/s). In these simulations, the performance improvement observed by adding broadside HH backscatter capability ($NRCS_{HH}$, 4base_RSVnan, black dashed line) is similar to the improvements obtained by adding broadside VV RSV capability (RSV_{VV}, 3base_RSV40, green solid line). The further addition of broadside RSV_{HH} (4base_RSV40, green dashed line) leads to only marginal further improvements across the swath (<0.01 m/s).

Instrument configurations "2base" and "3sq29" do not satisfy the 0.1 m/s mission requirements for TSCV over most of the swath and generally perform worse than other configurations, except at near range [−50 km, 0 km]. The reduced squint configuration (Figure 8, 3sq29_RSVnan, blue solid line) performs better than the baseline in near range, mainly because the broadside beam samples much larger incidence angles than the baseline (Table 2), hence obtaining better NRCS sensitivity to wind direction. We do not explain yet fully why the two-azimuth configuration (2base, black dotted line) performs better than the baseline (3base_RSVnan, black solid line) at very-near range [−50 km, −20 km] given that there is no broadside data and the squinted beams have the same incidence and azimuth angles as the baseline configuration. One hypothesis is that the retrieval has some non-linearities at the very-near range.

The TSCV performance for individual wind directions for the six scenarios is presented in the appendix (Figure A5). The results for the "3base" and "4base" configurations are consistent with earlier findings with the baseline in Section 3.5, namely a marked TSCV performance degradation at near range in some wind directions around 270°. The addition of broadside RSV (3base_RSV40, 4base_RSV40) or broadside HH backscatter capability (4base_RSVnan) mitigates this effect a little, leading to the slightly better overall performance seen in Figure 8 for these configurations. The "2base" and "3sq29_RSVnan" configurations both show greater variability in performance with wind direction, including in sectors away from 270°.

To summarise, this analysis of different instrument configurations confirms the SeaSTAR baseline as a good trade-off that satisfies the mission's TSCV performance requirements without undue additional complications of the payload. The results demonstrate the benefits of an ASCAT-like geometry with three beams pointing 45° apart in azimuth compared to configurations with lower azimuth diversity (e.g., 3sq29_RSVnan). The addition of broadside RSV or broadside HH capability provides minor performance improvements, notably at near range, but increase payload complexity that could impact the viability of the mission in terms of mass and power budgets and cost.

5. Discussion and Conclusions

This paper outlines the numerical framework and simultaneous inversion scheme that were used during ESA Earth Explorer 11 (EE11) Phase 0 to estimate the SeaSTAR L2 retrieval performance for TSCV and OCVW for different ocean current and wind conditions, and different instrument configurations, geometries and L1B noise specifications. The work builds on earlier research by Martin et al. [9], who developed the approach for a two-azimuth squinted along-track SAR interferometer with L1B noise characteristics (squinted NRCS Kp = 5% or 12%, squinted ΔRSV = 0.04 or 0.1 m/s, equivalent to Doppler frequency noise of 2 or 5 Hz) that differed slightly from those considered here. Martin et al. [9] revealed limitations of the two-azimuth design for high-accuracy TSCV retrieval at low winds when the wind direction aligns with one of the instrument's two azimuth lines-of-sight. The study also recommended maintaining incidence angles for squinted beams above 35° and the need for low noise L1B NRCS. Based on these considerations and drawing from insights about wind direction sensitivity by Stoffelen and Portabella [11], the SeaSTAR concept was born, with an ASCAT-like three-azimuth design that incorporates a broadside antenna to enhance wind direction sensitivity.

The key characteristics of the SeaSTAR baseline design developed in EE11 Phase 0 are detailed in Section 2 and Table 1. The concept features: (1) an ASCAT-like viewing geometry with three beams pointing about 45° apart in azimuth that provide optimal azimuth diversity in NRCS; (2) moderate incidence angles for squinted beams between 31.5° and 40°; (3) low L1B noise on NRCS with Kp = 3% in squinted directions and 4% broadside. (4) a demanding requirement for low L1B noise on RSV in the squinted directions, with ΔRSV = 0.07 m/s found sufficient to achieve the mission's L2 performance requirements.

The retrieval performance for L2 TSCV and OSVW of the SeaSTAR baseline concept was evaluated for idealised uniform vectorial fields of ocean currents and surface winds (Section 4.1) and realistic conditions over Iroise Sea (Section 4.2). Notably, the simulations with realistic 2D fields over the Iroise Sea showcased SeaSTAR's remarkable ability to correctly recover the structures and magnitudes of fine-scale ocean current and wind fields in complex oceanographic conditions (Figure 1, Section 4.2). Simulations with idealised uniform TSCV and OSVW fields demonstrate SeaSTAR's ability to meet the mission L2 performance requirements even in low wind conditions (5 m/s), with mean RMSE for TSCV and OSVW, respectively, better than 0.1 and 0.4 m/s over most of the swath. The baseline design still presents performance degradation in parts of the swath at near range for low wind speeds and wind directions around 270° (relative to satellite heading), pointing to some remaining questions about wind direction sensitivity in these specific conditions. The performance degradation under these specific conditions is well understood. In future work, we will associate uncertainty estimates with the retrievals. These uncertainties will subsequently be integrated into higher-level processors to ensure consistent performance.

Section 4.3 presents an assessment of L2 TSCV performance for six instrument configurations centred on and around the baseline design. This served to quantify the impact on the performance of various instrument trade-offs and to refine the requirements for the mission and payload in EE11 Phase 0. The analyses demonstrate the benefits of an ASCAT-like geometry with three beams pointing 45° apart in azimuth compared to configurations with lower azimuth diversity (as in the case of reduced squint angle (3sq29_RSVnan). Our results also underscore the rapid non-linear degradation of performance when moving to steeper incidence angles compared to the baseline, equivalent to a requirement for a minimum broadside incidence angle of 20°.

Within the assumptions of our simulation framework, we find that the addition of broadside RSV or broadside HH capability would provide only small or marginal performance improvements ($\sim$0.01 m/s), mostly at near range. These findings should be nuanced by recognising the limitations of the GMFs used in the inversion, and that broadside RSV and HH NRCS data have considerable scientific value aside from their use to improve retrieval performance. Importantly, high-resolution broadside RSV or HH data would provide valuable additional information to detect and quantify localised ocean surface signatures, notably linked to the wind/wave/current interactions and the modification of surface waves and wave breaking by dynamic oceanographic and atmospheric fronts, as shown in studies such as Kudryavtsev et al. [31] and Mouche and Chapron [32]. Thus, our simulations alone do not provide sufficient evidence to abandon the aspiration of including broadside RSV and/or broadside HH capability in future designs.

This work raises a number of questions in need of further investigation. For example, our performance estimation is based on the SeaSTAR simultaneous retrieval of TSCV and OSVW, which explicitly accounts for the coupling between wind and current vectors. However, we acknowledge that alternative inversion approaches, such as sequential or iterative methods, have been proposed in various other contexts. It follows that an intercomparison should be performed to comprehensively assess the performance, limitations and respective merits of different approaches.

Likewise, the issue of ambiguity removal deserves further scrutiny. As mentioned in Section 3.4, advanced techniques have evolved in scatterometry to mitigate ambiguities among the four solutions; for example, by introducing external constraints derived from the characteristics of the resulting wind field, including higher-order spatial properties like rotation and divergence (OSI SAF, 2022 [33]). These mature techniques hold the potential to be applied to SeaSTAR data, warranting further exploration and investigation as part of future research endeavours.

Additionally, the impact of rain contamination on SeaSTAR's performance must be addressed. At Ku-band, rain increases backscatter from the rain column and rain-induced surface roughening, leading to positive biases in wind speed retrievals [2]. Furthermore, rain-enhanced backscatter can degrade along-track interferometry coherence and Doppler phase measurements. Future research should focus on developing strategies to accurately estimate and mitigate these rain-induced effects to ensure the robustness of SeaSTAR's retrievals under such conditions.

Lastly, further work is needed to improve our understanding of microwave Doppler measurements from the ocean and refine geophysical models. A growing body of evidence highlights the benefits of incorporating sea state information alongside wind vector parameterisations in geophysical models, as demonstrated by Moiseev et al. [20] and Martin et al. [24]. In this work, the L2 inversion does not account for sea state. Future investigations should explore how the inversion could integrate some of the sea state information that SeaSTAR will derive from its broadside and squinted beam images (e.g., directional swell spectrum, significant wave height). This would make it possible to evaluate whether incorporating additional information further enhances the retrieval performance and how it might change the sensitivity of the retrieval to wind direction.

Author Contributions: Conceptualisation, A.C.H.M. and C.P.G.; methodology, A.C.H.M. and C.P.G.; software development, A.C.H.M.; simulation runs, A.C.H.M. and D.A.; formal analysis, A.C.H.M. and C.P.G.; technical input on SeaSTAR, P.M.-I. and A.E.; writing—original draft preparation, A.C.H.M.; writing—review and editing, A.C.H.M. and C.P.G.; visualization, A.C.H.M. and D.A.; funding

acquisition, C.P.G. and A.C.H.M. All authors have read and agreed to the published version of the manuscript.

Funding: This work was part-funded by the ESA Earth Explorer 11 Phase 0 Science and Requirements Consolidation Study (SciReC-SEASTAR, ESA EXPRO RFP/3-17308/21/NL/FF/ab), with additional financial and material support from the National Oceanography Centre, the Centre for Earth Observation Instrumentation (ceoi.ac.uk), the Natural Environment Research Council (nerc.ukri.org) and the ESA Feasibility Study into Next Generation Scatterometers (ESA AO/1-12048/24/NL/FFi).

Data Availability Statement: The data outputs generated from the simulations and analysis described in this study are publicly available through the SciRec data repository. The dataset includes simulation inputs and outputs in netCDF. This dataset also includes a Python notebook with the data analysis including figures presented in this paper. The data can be accessed at https://github.com/ACHMartin/SciRec/releases/tag/v1.0 (accessed on 31 July 2024)

Conflicts of Interest: Author Daria Andrievskaia was employed by the company NOVELTIS. The remaining authors declare that the research was conducted in the absence of any commercial or financial relationships that could be construed as a potential conflict of interest.

Abbreviations

The following abbreviations are used in this manuscript:

EE11	ESA Earth Explorer 11 programme
ESA	European Space Agency
GMF	Geophysical Model Function
NRCS	Normalised Radar Cross Section
OSVW	Ocean Surface Vector Wind
RMSE	Root Mean Square Error
RSV	Radial Surface Velocity
TSCV	Total Surface Current Vector
WASV	Wind-wave Artefact Surface Velocity

Appendix A

This appendix includes complementary materials. Figures A1–A3 extend what is presented in Figure 4 but for the SeaSTAR phase 0 configuration as defined in Table 1 and for a full matrix of wind (5, 9, 15 m/s) and range (near, mid, far). Figure A5 is the same as Figure 6-left but for the different instrument variations defined in Section 4.3. The different curves in Figure 8 are the black solid line of all instrument variations shown in Figure A5.

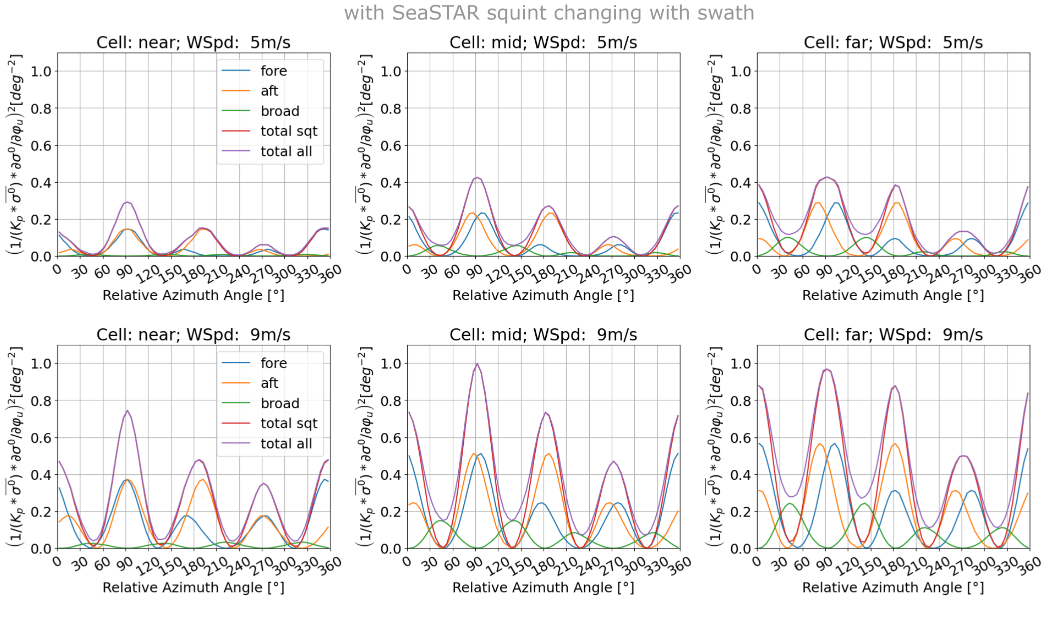

Figure A1. *Cont.*

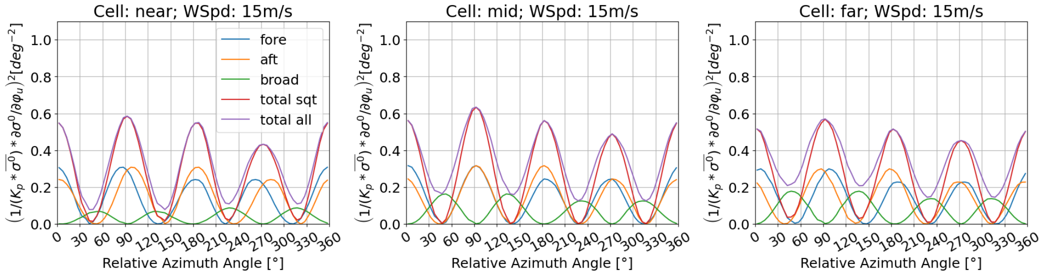

Figure A1. Sensitivity of NRCS to relative wind direction ($\partial\sigma^0/\partial\varphi_u$), with φ_u denoting the wind direction, relative to the satellite's north-heading, at, respectively, (1st row) 5 m/s, (2nd row) 9 m/s and (last row) 15 m/s wind speed for a range corresponding to incidence angle for the broadside beam of (left) 20°, (mid) 28.4°, (right) 33.4°. Squinted antennas are oriented for SeaSTAR phase 0 as defined in Table 1. Same legend as in Figure 4.

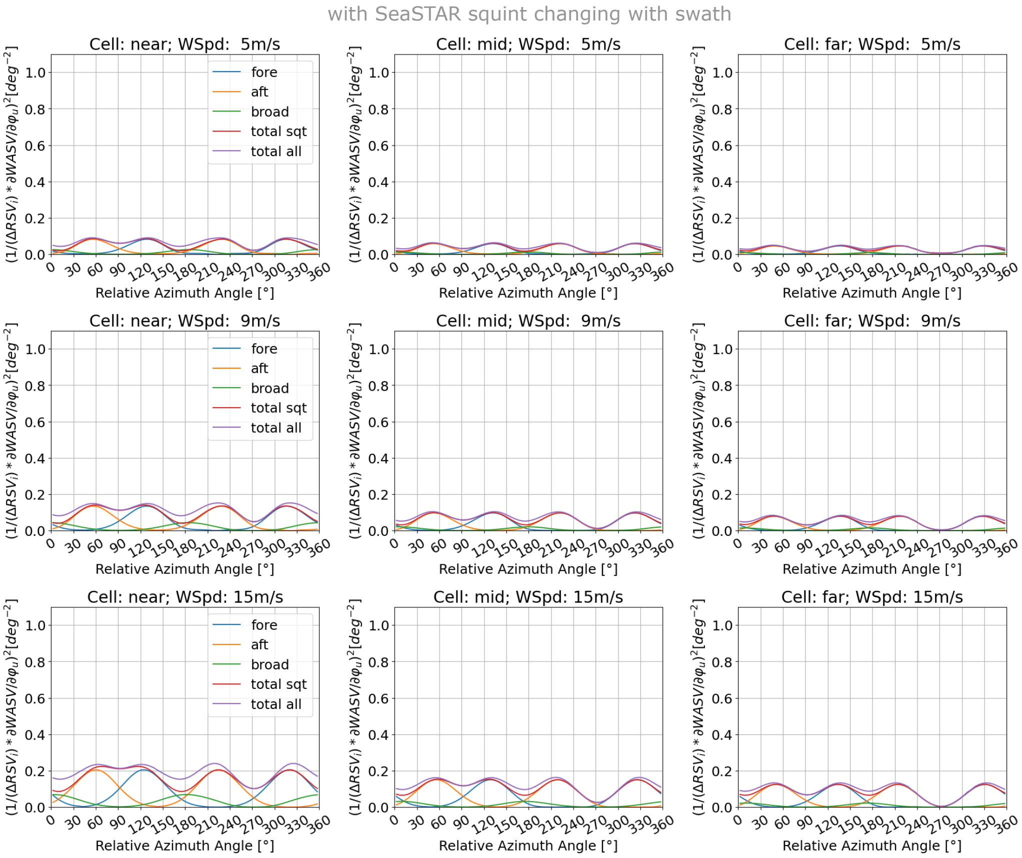

Figure A2. Sensitivity of RSV/WASV to relative wind direction ($\partial RSV/\partial\varphi_u$), with φ_u denoting the wind direction, relative to the satellite's north-heading, at, respectively, (1st row) 5 m/s, (2nd row) 9 m/s and (last row) 15 m/s wind speed for a range corresponding to incidence angle for the broadside beam of (left) 20°, (mid) 28.4°, (right) 33.4°. Squinted antennas are oriented for SeaSTAR phase 0 as defined in Table 1. Same legend as in Figure 4.

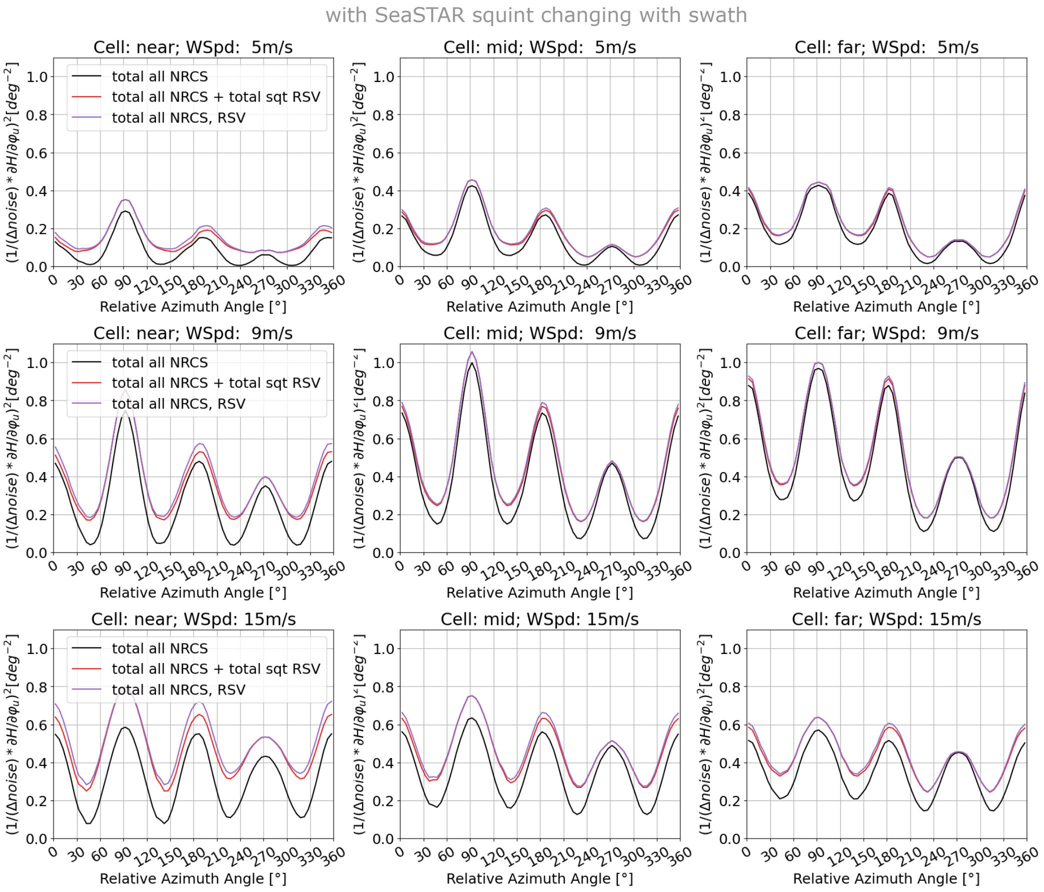

Figure A3. Sensitivity of combined NRCS + WASV to relative wind direction ($\partial\sigma^0/\partial\varphi_u$ and $\partial RSV/\partial\varphi_u$), with φ_u denoting the wind direction, relative to the satellite's north-heading, at, respectively, (1st row) 5 m/s, (2nd row) 9 m/s and (last row) 15 m/s wind speed for at range corresponding to incidence angle for the broadside beam of (left) 20°, (mid) 28.4°, (right) 33.4°. Squinted antennas are oriented for SeaSTAR phase 0 as defined in Table 1. Same legend as in Figure 4.

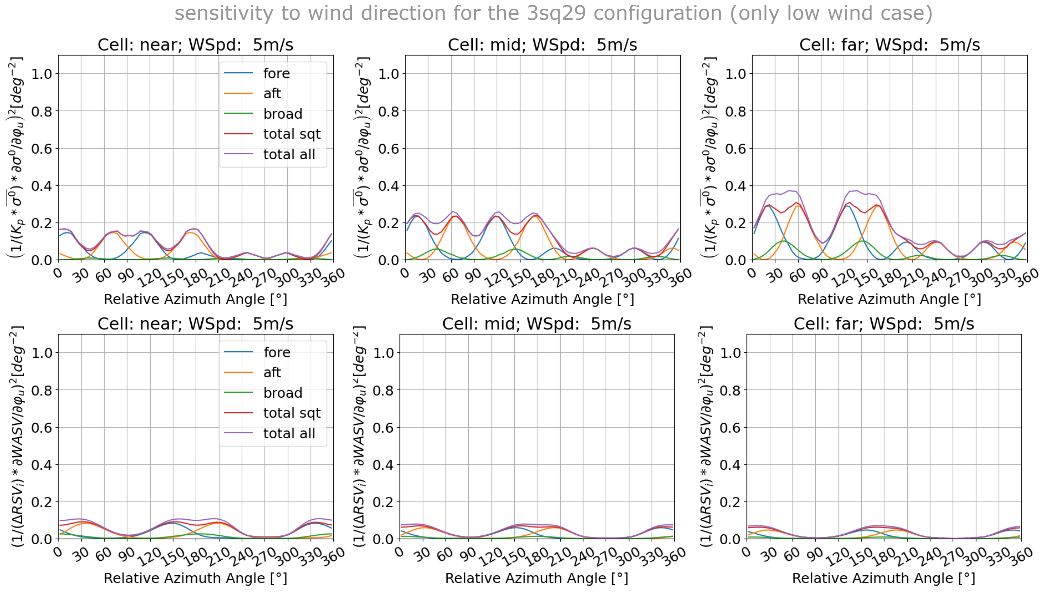

Figure A4. *Cont.*

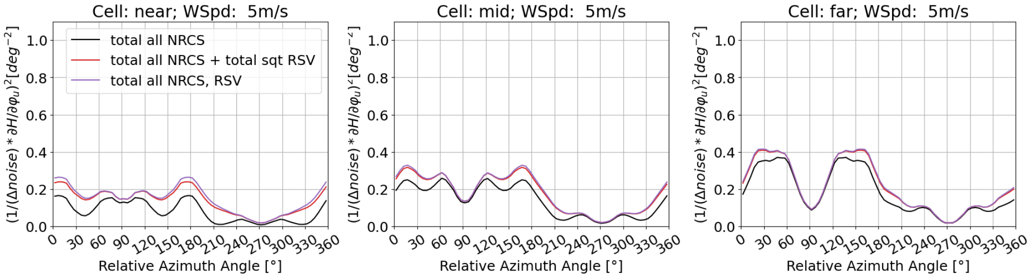

Figure A4. Sensitivity of (top) NRCS, (middle) WASV, (bottom) combined NRCS + WASV to relative wind direction ($\partial\sigma^0/\partial\varphi_u$ and $\partial RSV/\partial\varphi_u$), with φ_u denoting the wind direction, relative to the satellite's north-heading, for a low wind speed of 5 m/s at range corresponding to incidence angle for the broadside beam of (left) 20°, (mid) 28.4°, (right) 33.4°. Squinted antennas are oriented as for "Squint29" as defined in Table 2. Same legend as in Figure 4.

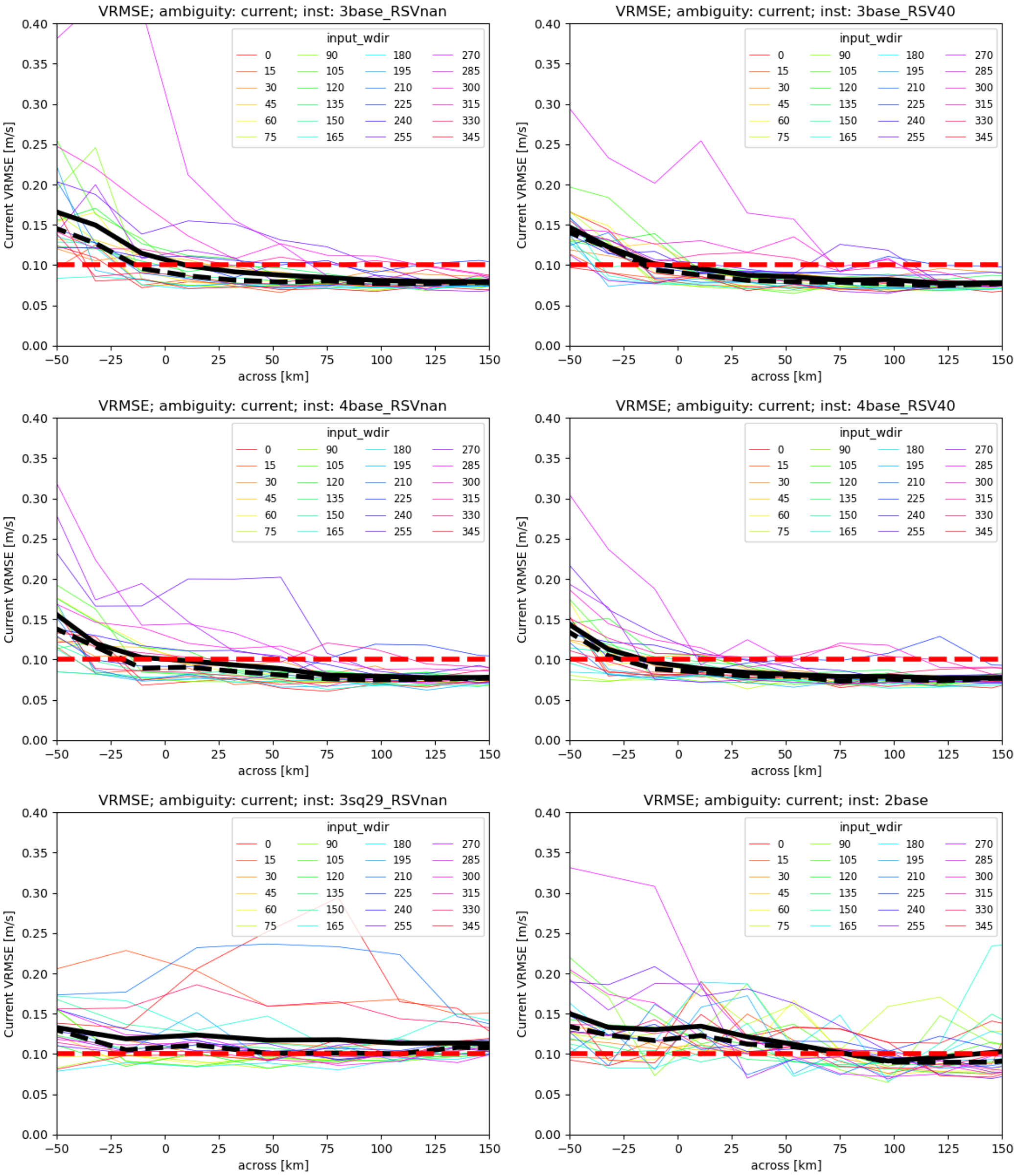

Figure A5. Same as Figure 6-left but for the different instrument variations defined in Section 4.3. Instrument configurations are indicated in each figure's header.

References

1. Ballarotta, M.; Ubelmann, C.; Pujol, M.I.; Taburet, G.; Fournier, F.; Legeais, J.F.; Faugere, Y.; Delepoulle, A.; Chelton, D.; Dibarboure, G.; et al. On the resolutions of ocean altimetry maps. *Ocean. Sci. Discuss.* **2019**, *2019*, 1–27. [CrossRef]
2. Bourassa, M.A.; Meissner, T.; Cerovecki, I.; Chang, P.S.; Dong, X.; De Chiara, G.; Donlon, C.; Dukhovskoy, D.S.; Elya, J.; Fore, A.; et al. Remotely Sensed Winds and Wind Stresses for Marine Forecasting and Ocean Modeling. *Front. Mar. Sci.* **2019**, *6*, 443 [CrossRef]
3. Ardhuin, F.; Aksenov, Y.; Benetazzo, A.; Bertino, L.; Brandt, P.; Caubet, E.; Chapron, B.; Collard, F.; Cravatte, S.; Delouis, J.M.; et al. Measuring currents, ice drift, and waves from space: The Sea surface KInematics Multiscale monitoring (SKIM) concept. *Ocean. Sci.* **2018**, *14*, 337–354. [CrossRef]
4. Rodríguez, E.; Bourassa, M.; Chelton, D.; Farrar, J.T.; Long, D.; Perkovic-Martin, D.; Samelson, R. The Winds and Currents Mission Concept. *Front. Mar. Sci.* **2019**, *6*, 438. [CrossRef]
5. Lopez-Dekker, P.; Rott, H.; Prats-Iraola, P.; Chapron, B.; Scipal, K.; Witte, E.D. Harmony: An Earth Explorer 10 Mission Candidate to Observe Land, Ice, and Ocean Surface Dynamics. In Proceedings of the IGARSS 2019—2019 IEEE International Geoscience and Remote Sensing Symposium, Yokohama, Japan, 28 July 2019–2 August 2019. [CrossRef]
6. Gommenginger, C.P.; Hall, K.; Casal, T.; Martin-Inglesias, P.; Cipollini, P.; Martin, A.C.H.; Team, I.S. Small-Scale Ocean Surface Dynamics from Space: The Earth Explorer 11 Candidate Mission Seastar. In Proceedings of the ESA Living Planet Symposium, Bonn, Germany, 23–27 May 2022.
7. Torres, H.; Wineteer, A.; Klein, P.; Lee, T.; Wang, J.; Rodriguez, E.; Menemenlis, D.; Zhang, H. Anticipated Capabilities of the ODYSEA Wind and Current Mission Concept to Estimate Wind Work at the Air–Sea Interface. *Remote Sens.* **2023**, *15*, 3337. [CrossRef]
8. Gommenginger, C.; Chapron, B.; Hogg, A.; Buckingham, C.; Fox-Kemper, B.; Eriksson, L.; Soulat, F.; Ubelmann, C.; Ocampo-Torres, F.; Nardelli, B.B.; et al. SEASTAR: A Mission to Study Ocean Submesoscale Dynamics and Small-Scale Atmosphere-Ocean Processes in Coastal, Shelf and Polar Seas. *Front. Mar. Sci.* **2019**, *6*, 457. [CrossRef]
9. Martin, A.C.; Gommenginger, C.P.; Quilfen, Y. Simultaneous ocean surface current and wind vectors retrieval with squinted {SAR} interferometry: Geophysical inversion and performance assessment. *Remote Sens. Environ.* **2018**, *216*, 798–808. [CrossRef]
10. Schyberg, H.; Breivik, L.A. Objective analysis combining observation errors in physical space and observation space. *Q. J. R. Meteorol. Soc.* **2002**, *128*, 695–711. [CrossRef]
11. Stoffelen, A.; Portabella, M. On Bayesian scatterometer wind inversion. *IEEE Trans. Geosci. Remote Sens.* **2006**, *44*, 1523–1533. [CrossRef]
12. Mouche, A.; Collard, F.; Chapron, B.; Dagestad, K.; Guitton, G.; Johannessen, J.; Kerbaol, V.; Hansen, M. On the Use of Doppler Shift for Sea Surface Wind Retrieval From SAR. *IEEE Trans. Geosci. Remote Sens.* **2012**, *50*, 2901–2909. [CrossRef]
13. Elyouncha, A.; Eriksson, L.E.; Broström, G.; Axell, L.; Ulander, L.H. Joint retrieval of ocean surface wind and current vectors from satellite SAR data using a Bayesian inversion method. *Remote Sens. Environ.* **2021**, *260*, 112455. [CrossRef]
14. Martin, A.C.H.; Gommenginger, C.; Marquez, J.; Doody, S.; Navarro, V.; Buck, C. Wind-Wave induced velocity in ATI SAR Ocean Surface Currents: First experimental evidence from an airborne campaign. *J. Geophys. Res. Ocean.* **2016**, *121*, 1640–1653. [CrossRef]
15. Wentz, F.J.; Smith, D.K. A model function for the ocean-normalized radar cross section at 14 GHz derived from NSCAT observations. *J. Geophys. Res. Ocean.* **1999**, *104*, 11499–11514. [CrossRef]
16. Ricciardulli, L.; Wentz, F.J. A Scatterometer Geophysical Model Function for Climate-Quality Winds: QuikSCAT Ku-2011. *J. Atmos. Ocean. Technol.* **2015**, *32*, 1829–1846. [CrossRef]
17. Wang, Z.; Stoffelen, A.; Zhang, B.; He, Y.; Lin, W.; Li, X. Inconsistencies in scatterometer wind products based on ASCAT and OSCAT-2 collocations. *Remote Sens. Environ.* **2019**, *225*, 207–216. [CrossRef]
18. Royal Netherlands Meteorological Institute. *NSCAT-4DS Geophysical Model Function*; Royal Netherlands Meteorological Institute: Utrecht, The Netherlands, 2019.
19. Yurovsky, Y.; Kudryavtsev, V.; Grodsky, S.; Chapron, B. Sea Surface Ka-Band Doppler Measurements: Analysis and Model Development. *Remote Sens.* **2019**, *11*, 839. [CrossRef]
20. Moiseev, A.; Johnsen, H.; Johannessen, J.A.; Collard, F.; Guitton, G. On Removal of Sea State Contribution to Sentinel-1 Doppler Shift for Retrieving Reliable Ocean Surface Current. *J. Geophys. Res. Ocean.* **2020**, *125*, e2020JC016288. [CrossRef]
21. Moiseev, A.; Johannessen, J.A.; Johnsen, H. Towards Retrieving Reliable Ocean Surface Currents in the Coastal Zone From the Sentinel-1 Doppler Shift Observations. *J. Geophys. Res. Ocean.* **2022**, *127*, e2021JC018201. [CrossRef]
22. Fois, F.; Hoogeboom, P.; Le Chevalier, F.; Stoffelen, A. An analytical model for the description of the full polarimetric sea surface Doppler signature. *J. Geophys. Res. Ocean.* **2015**, *120*, 988–1015. [CrossRef]
23. Elyouncha, A.; Eriksson, L.E.; Johnsen, H. Direct comparison of sea surface velocity estimated from Sentinel-1 and TanDEM-X SAR data. *IEEE J. Sel. Top. Appl. Earth Obs. Remote Sens.* **2022**, *15*, 2425–2436. [CrossRef]
24. Martin, A.C.; Gommenginger, C.P.; Jacob, B.; Staneva, J. First multi-year assessment of Sentinel-1 radial velocity products using HF radar currents in a coastal environment. *Remote Sens. Environ.* **2022**, *268*, 112758. [CrossRef]
25. Portabella, M. Wind Field Retrieval from Satellite Radar Systems. Ph.D. Thesis, Departament d'Astronomia i Meteorologia, Universitat de Barcelona, Barcelona, Spain, 2002.

26. Vogelzang, J.; Stoffelen, A. Improvements in Ku-band scatterometer wind ambiguity removal using ASCAT-based empirical background error correlations. *Q. J. R. Meteorol. Soc.* **2018**, *144*, 2245–2259. [CrossRef]
27. Chi, C.Y.; Li, F. A comparative study of several wind estimation algorithms for spaceborne scatterometers. *IEEE Trans. Geosci. Remote Sens.* **1988**, *26*, 115–121. [CrossRef]
28. Lin, C.C.; Betto, M.; Rivas, M.B.; Stoffelen, A.; de Kloe, J. EPS-SG Windscatterometer Concept Tradeoffs and Wind Retrieval Performance Assessment. *IEEE Trans. Geosci. Remote Sens.* **2012**, *50*, 2458–2472. [CrossRef]
29. Fisher, N.I. *Statistical Analysis of Circular Data*; Cambridge University Press: Cambridge, UK, 1995.
30. McCann, D.L.; Martin, A.C.H.; Macedo, K.; Carrasco, R.; Horstmann, J.; Marié, L.; Marquez, J.; Meta, A.; Gommenginger, C.; Martin-Iglesias, P.; et al. A new airborne system for simultaneous high-resolution ocean vector current and wind mapping: First demonstration of the SeaSTAR mission concept in the macrotidal Iroise Sea. *Ocean. Sci.* **2024**, *20*, 1109–1122. [CrossRef]
31. Kudryavtsev, V.; Kozlov, I.; Chapron, B.; Johannessen, J.A. Quad-polarization SAR features of ocean currents. *J. Geophys. Res. Ocean.* **2014**, *119*, 6046–6065. [CrossRef]
32. Mouche, A.; Chapron, B. Global C-Band Envisat, RADARSAT-2 and Sentinel-1 SAR measurements in copolarization and cross-polarization. *J. Geophys. Res. Ocean.* **2015**, *120*, 7195–7207. [CrossRef]
33. Vogelzang, J. *Two-Dimensional Variational Ambiguity Removal (2DVAR)*; Techreport Version 1.8, NWP SAF; KNMI: De Bilt, The Netherlands, 2022; NWPSAF-KN-TR-004.

Disclaimer/Publisher's Note: The statements, opinions and data contained in all publications are solely those of the individual author(s) and contributor(s) and not of MDPI and/or the editor(s). MDPI and/or the editor(s) disclaim responsibility for any injury to people or property resulting from any ideas, methods, instructions or products referred to in the content.